Behavioral/Systems/Cognitive

Spatial Profile and Differential Recruitment of GABA$_B$ Modulate Oscillatory Activity in Auditory Cortex

Anne-Marie M. Oswald,[1]* **Brent Doiron,**[1,2]* **John Rinzel,**[1,2] **and Alex D. Reyes**[1]

[1]Center for Neural Science and [2]Courant Institute of Mathematical Sciences, New York University, New York, New York 10003

The interplay between inhibition and excitation is at the core of cortical network activity. In many cortices, including auditory cortex (ACx), interactions between excitatory and inhibitory neurons generate synchronous network gamma oscillations (30–70 Hz). Here, we show that differences in the connection patterns and synaptic properties of excitatory–inhibitory microcircuits permit the spatial extent of network inputs to modulate the magnitude of gamma oscillations. Simultaneous multiple whole-cell recordings from connected fast-spiking interneurons and pyramidal cells in L2/3 of mouse ACx slices revealed that for intersomatic distances <50 μm, most inhibitory connections occurred in reciprocally connected (RC) pairs; at greater distances, inhibitory connections were equally likely in RC and nonreciprocally connected (nRC) pairs. Furthermore, the GABA$_B$-mediated inhibition in RC pairs was weaker than in nRC pairs. Simulations with a network model that incorporated these features showed strong, gamma band oscillations only when the network inputs were confined to a small area. These findings suggest a novel mechanism by which oscillatory activity can be modulated by adjusting the spatial distribution of afferent input.

Introduction

The responses of cortical neurons to sensory stimuli are strongly influenced by the recruitment of inhibition during network activity. Fast-spiking (FS) interneurons have a high probability of connection with pyramidal cells (PCs) and are thus a major source of intracortical inhibition (Thomson et al., 1996; Gonchar and Burkhalter, 1999; Beierlein et al., 2003; Holmgren et al., 2003). FS–PC circuitry has been implicated in tuning receptive fields and dampening cortical responses (Gonchar and Burkhalter, 1999; Beierlein et al., 2003; Swadlow, 2003; Sun et al., 2006; Atencio and Schreiner, 2008). In addition, experimental (Buhl et al., 1998; Sukov and Barth, 2001; Hasenstaub et al., 2005; Morita et al., 2008) and theoretical investigations (Brunel and Wang, 2003; Cunningham et al., 2004; Börgers et al., 2005) have suggested that coupled networks of excitatory and inhibitory neurons support synchronous network oscillations. In the present study, we show how the spatial pattern of connectivity in FS–PC microcircuits influences the recruitment of inhibition and modulates oscillatory activity.

Oscillations in the gamma frequency range (~30–70 Hz) have been correlated with specific stimuli in auditory cortex (ACx) (Barth and MacDonald, 1996; Sukov and Barth, 2001; Brosch

et al., 2002), as well as other sensory systems [somatosensory (Jones and Barth, 2002); visual (Gray and Singer, 1989); olfactory (Laurent et al., 1996); electrosensory (Doiron et al., 2003)]. Moreover, gamma activity in ACx is modulated by site-specific stimulation of auditory thalamus (Barth and MacDonald, 1996; Metherate and Cruikshank, 1999; Sukov and Barth, 2001), cross-modal activation of somatosensory and visual thalamocortical pathways (Lakatos et al., 2005, 2007), and selective attention to auditory stimuli (Lakatos et al., 2004). Responses to acoustic stimuli in ACx are tonotopically ordered (Stiebler et al., 1997; Schreiner et al., 2000; Schreiner and Winer, 2007), which suggests a spatial organization of inputs and circuitry within ACx could impart specificity and modulation of gamma oscillations.

Gamma oscillations are most prominent in the upper layers (L2–L4) of ACx (Metherate and Cruikshank, 1999; Cunningham et al., 2004; Lakatos et al., 2005) and may be mediated by PC and FS cell interactions (Sukov and Barth, 2001). Although the properties of FS–PC circuitry have been characterized in other sensory systems (Thomson et al., 1996; Markram et al., 1998; Reyes et al., 1998; Gupta et al., 2000; Thomson et al., 2002; Holmgren et al., 2003), comparable studies have not been conducted in ACx. We investigated the spatial distribution and synaptic properties of inhibitory connections between PC and FS cells in L2/3 of ACx. When the somata of FS–PC pairs were separated by <50 μm, most inhibitory connections occurred in reciprocally connected (RC) pairs. For longer distances (50–100 μm), RC and nonreciprocally connected (nRC) FS–PC pairs occurred with equal probability. In addition, PCs in RC pairs received less GABA$_B$-mediated inhibition than those in nRC pairs. We incorporated these results in a spiking network model and found maximal gamma oscillatory power for network inputs with a spatial profile that coincided with the ~50 μm region dominated by RC pairs. Inputs that activated larger network areas recruited more

GABA$_B$-mediated inhibition and reduced oscillatory activity. Our results suggest that the connectivity profile and the recruitment of inhibition within FS–PC circuits allow the spatial profile of inputs to L2/3 to modulate gamma oscillations in ACx.

Materials and Methods

Experiments

Slice preparation. Auditory thalamocortical slices were prepared from Swiss Webster mice [postnatal day 14 (P14) to P29] as described by Cruikshank et al. (2002). All surgical procedures followed the guidelines determined by the New York University Animal Welfare Committee. Mice were anesthetized with halothane and decapitated. The brain was exposed and two coronal cuts were made to remove the anterior 25% of the brain and the cerebellum. The brain was then removed from the skull and immersed, anterior cut down, in ice-cold oxygenated (95% O$_2$–5% CO$_2$) artificial CSF (ACSF) (in mM: 125 NaCl, 2.5 KCl, 25 NaHCO$_3$, 1.25 NaH$_2$PO$_4$, 1.0 MgCl$_2$, 25 dextrose, 2 CaCl$_2$) (all chemicals from Sigma-Aldrich). A third cut was made with a ~15° medial-to-lateral slant to remove the dorsal portion of the brain leaving one hemisphere intact. The brain was submerged in ice-cold ACSF, and horizontal slices (300 μm) were made using a vibratome (Campden Instruments). Typically, one or two slices contained primary ACx, the medial geniculate nucleus (MG), and the thalamocortical fiber tract. The slices were maintained in ACSF at 37°C for 30 min, and then rested at room temperature (20–22°C) for 1–2 h before recording (29–33°C).

Electrophysiology. Neurons were visualized using infrared-differential interference contrast microscopy (Olympus). At low magnification, the MG was visible medial to the hippocampus and posterior to the lateral geniculate nucleus, and ACx was located lateral to the anterior half of the hippocampus (Cruikshank et al., 2002). L2/3 was the cell-dense region 100–300 μm below the pia. Only slices containing the MG and ACx were used. In a subset of slices, the location of ACx was verified by stimulating the MG and recording field potential responses in L3/4. At higher magnification, PCs were identified by a distinct apical dendrite that extended toward L1, whereas FS cells were distinguished by ovoid somata and multipolar dendrites. Whole-cell current-clamp recordings were made simultaneously from up to four neurons (amplifier; Dagan; acquisition and analysis software; IgorPro; Wavemetrics). Voltage-clamp recordings were not performed because the addition of QX-314 (lidocaine *N*-ethyl bromide) or cesium to the recording pipette to improve space-clamp interferes with potassium channels and, consequently, with recordings of GABA$_B$. In the absence of adequate space clamp, the results of voltage-clamp recordings would not be expected to differ from current clamp. Recorded neurons were located two to four cell layers (40–70 μm) below the surface of the slice. Pipettes were pulled from borosilicate glass (2.0 outer diameter) on a Flaming/Brown micropipette puller (Sutter Instrument) to a resistance of 3–10 MΩ. The intracellular solution consisted of the following (in mM): 130 K-gluconate, 5 KCl, 2 MgCl$_2$, 4 ATP-Mg, 0.3 GTP, 10 HEPES, and 10 phosphocreatine.

Stimulation. We recorded from 143 PCs and 101 FS cells. A series of hyperpolarizing and depolarizing step currents (1 s in duration) were injected to measure the input resistance, time constant, and action potential responses of each cell. For the FS cells, the average membrane time constant was 7 ± 3 ms, the input resistance was 122 ± 44 MΩ and the resting membrane potential was −71 ± 4 mV. To quantify spike frequency adaptation in FS cells, we measured the ratio of the last interspike interval (ISI$_L$) to the first ISI (ISI$_F$) in response to a 1 s step current injection that evoked firing rates of 48 ± 15 Hz. The pertinent intrinsic properties of PCs are reported in Results and were consistent with previously reported values (Oswald and Reyes, 2008).

To determine whether FS–PC pairs were synaptically connected, one neuron of the pair was stimulated with five suprathreshold current pulses (0.5–1 nA; 5 ms pulse width) delivered at 10 Hz. Average membrane potential responses were compiled from 25 to 35 trials. In connected pairs, postsynaptic potentials (PSPs) that were temporally locked to the presynaptic action potential were evoked in the target cell. Connections in both directions (FS to PC; PC to FS) were tested. For each FS–PC pair, one of four connection patterns was possible:

not connected, unidirectional excitatory, unidirectional inhibitory, and reciprocally connected (both an excitatory and an inhibitory connection). In FS–PC pairs that had an inhibitory connection, the FS cell was driven to fire action potentials at a rate of 80 Hz for 500 ms while IPSPs were recorded in the postsynaptic PC. Analyses were performed on the average PC membrane responses compiled from 10 to 20 trials. IPSP amplitudes were taken as the difference between the membrane voltage at the peak of the IPSP and the onset of the IPSP. Short-term synaptic depression was measured by dividing the amplitude of each IPSP by the amplitude of the first IPSP. The intertrial interval was sufficiently long (7 s) to ensure full recovery from short-term depression.

Pharmacology. In a subset of experiments ($n = 8$ triplets), recordings were performed in the presence of the AMPA/kainate receptor antagonist DNQX [6,7-dinitroquinoxaline-2,3(1*H*,4*H*)-dione] (20 μM; Sigma-Aldrich) and the GABA$_A$ receptor antagonist bicuculline (10 μM; Sigma-Aldrich). Although bicuculline can nonspecifically block calcium-mediated potassium channels (Johansson et al., 2001), the low concentration and the membrane potentials at which the inhibitory responses were recorded (−60 mV) make it unlikely that blockade of these channels confounds our results. In four pairs, 2-hydroxysaclofen (50 μM; Sigma-Aldrich) was also applied and blocked the isolated GABA$_B$ component of the response (supplemental Fig. 2, available at www.jneurosci.org as supplemental material).

Data analysis and statistics. The probability of connection (P_c) was calculated as the number of connected pairs (N_c) divided by the number of tested pairs (N_T): $P_c = N_c/N_T$. We obtained the P_c versus intersomatic distance by calculating $P_c \pm SE_p$ for 10, 20, or 30 μm bin sizes between 20 and 100 μm. Bin sizes were chosen such that $N_T > 30$ for each bin. Since the probabilities of connection are categorical data, the SE for proportional data, $SE_p = (P_c(1 - P_c)/N_T)^{1/2}$, was calculated from the binomial formula. The SE_p is an indicator of confidence about P_c given 1 SD of the distribution and the sample size. Fisher's exact tests were used for statistical comparisons of connection probabilities based on the number of connected and unconnected pairs for each condition.

Synaptic parameters are reported as mean ± SD. The Kolmogorov–Smirnov test for normal distributions was performed on all data sets and the data did not differ significantly from that predicted for a normal distribution ($p = 0.14–0.67$). Significance was assessed using two-tailed Student's *t* tests: paired *t* tests were used when the two pyramidal cells that shared common FS cell input (referred to as triplet recordings) and unpaired *t* tests were used for comparisons between the total populations of RC and nRC pairs. In small data sets ($n < 10$), significance was assessed using the nonparametric Wilcoxon rank test for paired data.

Biocytin fills. To verify cell identity, 0.5% biocytin was added to the intracellular solution. Slices were fixed in 4% paraformaldehyde for processing. The slices were rinsed with PBS, quenched with 1% H$_2$O$_2$ in a 10% MeOH–PBS solution, permeabilized in Triton X-100 and then exposed to avidin–peroxidase complex (ABC kit; Vector Laboratories). The slices were rinsed (with PBS) and reacted with 3,3-diaminobenzidine, and then rinsed again. Finally, slices were mounted onto slides with Flourmount for microscopy and cell reconstruction using Neurolucida tracing (MBF Bioscience).

Model

We simulated a two-dimensional square sheet of 900 (30 × 30) PCs and 225 (15 × 15) FS cells. Each cell *ij* was distinguished by its (*x*, *y*) position, where $x_{ij,\alpha} = i\Delta_a$, $y_{ij,\alpha} = j\Delta_a$ and its cell type α (α = PC, FS). The neuron spacing was $\Delta_{PC} = 5$ μm and $\Delta_{FS} = 10$ μm; this maintained the density of a three-dimensional cortical volume after compression to a cortical sheet. The *x* and *y* coordinates of all FS cells were shifted by $\Delta_{PC}/2$, so that PC and FS cells did not occupy same point in space. The area of the sheet represents 22,500 μm^2 (150 × 150 μm) of L2/3 in ACx.

PC–PC cell connections were randomly distributed over the population with PC$_{kl}$ connecting to PC$_{ij}$ with probability $P_{PC–PC}$ (see Fig. 5*A*, black curve). PC–PC connections were independently and uniformly distributed in space. In contrast, FS–PC connectivity was distributed as a

function of the distance $d = [(i\Delta_{PC} - k\Delta_{FS})^2 + (j\Delta_{PC} - l\Delta_{FS})^2]^{1/2}$ between FS–PC pairs. We randomly assigned one of four possible states: nonreciprocal PC to FS connection (see Fig. 5A, connection probability P_{nRCE}, green curve), nonreciprocal FS to PC connection (see Fig. 5A, connection probability P_{nRCI}, blue curve), reciprocal PC and FS connections (see Fig. 5A, connection probability P_{RC}, red curve), or no connections $(1 - P_{nRCE} - P_{nRCI} - P_{RC})$. The spatial profile of these probability distributions approximately matched the experimentally obtained distributions (compare Fig. 2A with Fig. 5A) in that, for $d < 50$ μm, RC pairs were of higher probability than nRC pairs (Fig. 5A). Note that the overall probability of an FS to PC connection $(P_{nRCI} + P_{RC})$ and PC to FS cell $(P_{nRCE} + P_{RC})$ was 0.5 and independent of d.

Each cell in the network is a leaky integrate-and-fire (LIF) neuron with the following dynamics:

$$C\frac{dV_{ij,\alpha}}{dt} = g_L(E_L - V_{\alpha,ij}) + g_{ij,\alpha}^{AMPA}(t)(E_{AMPA} - V_{ij,\alpha})$$

$$+ g_{ij,\alpha}^{GA}(t)(E_{GA} - V_{ij,\alpha}) + g_{ij,\alpha}^{GB}(t)(E_{GB} - V_{ij,\alpha}). \quad (1)$$

$V_{ij,\alpha}(t)$ is the membrane potential of cell ij,α. Spiking dynamics were governed by the standard spike-reset rule, so that when $V_{ij,\alpha}(t)$ equals the threshold value of -60 mV, $V_{ij,\alpha}$ was immediately reset to $V_{ij,\alpha} = -70$ mV, and a spike time for cell ij,α was recorded at time t. PCs had an absolute refractory period of 5 ms, whereas FS cells have a 2 ms refractory period. The leak conductance $g_L = 10$ nS, the leak reversal potential $E_L = -70$ mV, and the membrane capacitance $C = 0.25$ nF, yielded a passive membrane time constant $\tau = C/g_L = 25$ ms.

The excitatory AMPA input to neuron ij,α, consists of two terms as follows:

$$g_{ij,\alpha}^{AMPA}(t) = \bar{g}_{AMPA}\left(\sum_{kl} \lambda_{ij,\alpha}^{kl,PC} \sum_m K_{AMPA}(t - t_{kl,PC}^m)\right.$$

$$\left. + \sum_m K_{AMPA}(t - t_{ij,ext}^m)\right). \quad (2)$$

The first term on the right-hand side of Equation 2 is excitatory input from a presynaptic pyramidal cell, PC_{kl}, to a postsynaptic cell α_{ij}. If a synaptic connection existed between PC_{kl} and cell α_{ij}, $\lambda_{ij,\alpha}^{kl,PC}$ was 1, and otherwise it was 0. $t_{kl,PC}^m$ is the mth spike time of PC_{kl}. The second term in Equation 2 is the external excitatory input to the network. For simplicity, the external input times, $t_{ij,ext}^m$, were chosen from a Poisson process of rate ν_{ext}. We divided PC and FS cells into "driven" (D) and "nondriven" (ND) groups. For PC_D and FS_D cells, ν_{ext} was 5.5 and 3.5 kHz, respectively; all ND cells had $\nu_{ext} = 0.4$ kHz representing spontaneous background activity. All external inputs were uncorrelated across all cells in the network. In this study, we always set the number of PC_D neurons to $N_{E,D} = 64$, and FS_D cells to $N_{I,D} = 16$. Cell α_{ij} was randomly assigned to class D with probability $p_{D,\alpha} = N_{D,\alpha}/(L/\Delta_\alpha)^2$ if cell α_{ij} was within the square stimulus region of length, L, centered in the middle of the network (see Figs. 5, 6). Finally, both external and internal EPSCs had an α function time course, where $K_{AMPA}(s) = \theta(s)(s/\tau_{AMPA})e^{1-s/\tau_{AMPA}}$ with $\tau_{AMPA} = 2.5$ ms; $\theta(s)$ is the Heaviside function, where $\theta(s) = 1$ if $s > 0$, and otherwise $\theta(s) = 0$, $\bar{g}_{AMPA} = 0.147$ nS, and the reversal potential $E_{AMPA} = 0$ mV.

The remaining two terms in Equation 1 model inhibitory activity within the network and were applied only to the membrane dynamics of PC cells (there are no FS–FS connections). Notation for inhibitory inputs follows that introduced for the excitatory inputs. The GABA$_A$ (GA) conductance to PC_{ij} was as follows:

$$g_{ij,PC}^{GA}(t) = \bar{g}_{GA} \sum_{kl} \lambda_{ij,PC}^{kl,FS} \sum_m K_{GA}(t - t_{kl,FS}^m). \quad (3)$$

$K_{GA}(s)$ was an α function with $\tau_{GA} = 4$ ms, a maximal conductance of $\bar{g}_{GA} = 0.46$ nS and a reversal potential of $E_{GA} = -70$ mV. All FS to PC connections have the same GABA$_A$ component.

Motivated by the experimental results (see Figs. 3, 4), the GABA$_B$ contributions to PC_{ij} were set according to two subpopulations of FS

cells: RC or nRC. The total GABA$_B$ conductance received by PC_{ij} was as follows:

$$g_{ij,PC}^{GB}(t) = \sum_{kl} \sum_m K_{GB}(t - t_{kl,FS}^m)\,[\bar{g}_{GB}^{RC}\,\lambda_{ij,PC}^{kl,FS}\,\lambda_{kl,FS}^{ij,PC}$$

$$+ \bar{g}_{GB}^{nRC}\,\lambda_{ij,PC}^{kl,FS}(1 - \lambda_{kl,FS}^{ij,PC})]. \quad (4)$$

All GABA$_B$ IPSCs had the same $K_{GB}(s)$ time course with $\tau_{GB} = 75$ ms, and a reversal potential $E_{GB} = -90$ mV. If cell FS_{kl} was RC with PC_{ij} (i.e., $\lambda_{ij,PC}^{kl,FS}, \lambda_{kl,FS}^{ij,PC} = 1$), the maximal conductance was $\bar{g}_{GB}^{RC} = 0.0114$ nS; conversely, if it was nRC to PC_{ij} (i.e., $\lambda_{ij,PC}^{kl,FS}(1 - \lambda_{kl,FS}^{ij,PC}) = 1$), the maximal conductance was $\bar{g}_{GB}^{nRC} = 0.0343$ nS. The inhibitory synapses were assumed to be in a sustained depressed state.

Model simulations were performed on a desktop PC with interfaced Matlab-C (MEX) code (Mathworks) and a standard Euler time scheme, where $\Delta t = 0.02$ ms. Neurons in the PC_{ND} population rarely elicited action potentials (see Fig. 5D), and therefore, the dynamics of these cells were often not simulated. This greatly decreased simulation cost, and the results were not affected quantitatively.

Each LIF model cell, α_{ij}, in the network produced a sequence of spike-threshold crossing times indexed by m, $\{t_{ij,\alpha}^m\}_m$, from which we defined a spike train $y_{ij,\alpha}(t) = \sum_m \delta(t - t_{ij,\alpha}^m)$, where $\delta(x)$ is a δ function centered at x. We divided the network into four subnetworks: $Y_{\alpha,\beta}(t) = \sum_{ij,\alpha \in \beta} y_{ij,\alpha}(t)$ with $\alpha = PC$ or FS and $\beta = D$ or ND. The network has three sources of randomness: (1) the event times of the random external inputs $t_{ij,ext}^m$, (2) the network connectivity $\lambda_{ij,\alpha}^{kl,\alpha'}$ ($\alpha,\alpha' = PC,FS$), and (3) the chosen driven and nondriven cells. We denote expectations over these sources as $\langle\cdot\rangle_t$ and $\langle\cdot\rangle_{Net}$, respectively; the former is the average over time (1) and the latter an average over realizations of the network connectivity (2, 3). We performed 120 realizations of input and network connectivity. For a given realization of connectivity and input distribution, the firing rate of cell α_{ij} is $r_{ij,\alpha} = \langle y_{ij,\alpha}\rangle_t$, and the firing rate of subnetwork $\alpha\beta$ is $R_{\alpha\beta} = \langle Y_{\alpha\beta}\rangle_t$. Spectral estimates of spike activity were defined by the Fourier transforms of $y_{ij,\alpha}(t) - r_{ij,\alpha}$ and $Y_{\alpha\beta}(t) - R_{\alpha\beta}$, and written as $\tilde{y}_{ij,\alpha}(f)$ and $\tilde{Y}_{\alpha\beta}(f)$, respectively, where f is frequency (in hertz). To measure subnetwork spike-train rhythms, we considered the power- and cross-spectra of the subnetwork dynamics as follows:

$$S_{\alpha\beta;\alpha'\beta'}(f) = \frac{1}{\sqrt{R_{\alpha\beta}R_{\alpha'\beta'}}}\tilde{Y}_{\alpha\beta}(f)\tilde{Y}_{\alpha'\beta'}^*(f), \quad (5)$$

where $\tilde{Y}_{\alpha\beta}^*(f)$ is the complex conjugate of $\tilde{Y}_{\alpha\beta}(f)$. For $\alpha = \alpha'$ and $\beta = \beta'$, $S_{\alpha\beta;\alpha\beta}$ is the power spectrum of network $\alpha\beta$ and is real-valued and asymptotes to 1 at very high f. For reference, a network with Poisson firing statistics would have $S_{\alpha\beta;\alpha\beta}(f) = 1$ for all f. When $\alpha \neq \alpha'$ or $\beta \neq \beta'$, $S_{\alpha\beta;\alpha'\beta'}(f)$ is the cross-spectra between networks $\alpha\beta$, and $\alpha'\beta'$, for which we only show the real component, and asymptotes to 0 at high f. Finally, to measure the pairwise spike correlation between driven (D) E cells, PC_{ij} and PC_{kl}, we measure the spike train coherence as follows:

$$C_{ij,PC;kl,PC}(f) = \frac{\sqrt{|\tilde{y}_{ij,PC}(f)\tilde{y}_{kl,PC}^*(f)|}}{[\tilde{y}_{ij,PC}(f)\tilde{y}_{ij,PC}^*(f)][\tilde{y}_{kl,PC}(f)\tilde{y}_{kl,PC}^*(f)]}, \quad (6)$$

where $|\cdot|$ is the modulus. $C_{ij,PC;kl,PC}(f)$ is 0 for spike trains that are uncorrelated at frequency f, and 1 for spike trains completely correlated at frequency f.

Spectral estimates were computed with the MATLAB signal processing toolbox (Mathworks) using a Bartlett window and spike trains digitized at 2 kHz. For a fixed network architecture and input distribution, all spectral analyses were conducted on 70 s spike trains with the transient first second removed. In this study, we always show $\langle\cdot\rangle_{Net}$ with error estimates (see Figs. 6, 7, shaded regions) being 1 SD computed from the Net data ensemble (120 realizations).

Results

Whole-cell current-clamp recordings were made from morphologically and electrophysiologically identified neurons in L2/3 in a thalamocortical slice preparation of ACx (Cruikshank et al., 2002). Under infrared video-microscopy, PCs were distinguished

by a prominent apical dendrite that extended to L1, whereas FS cells had multipolar dendritic morphology (Fig. 1*A*). PCs responded to suprathreshold, constant current injections with a high-frequency spike doublet followed by lower frequency firing that ranged from 6 ± 4 Hz at rheobase (0.17 ± 0.1 nA) to 51 ± 15 Hz at higher current injections (Fig. 1*B*, left). In contrast, FS cells exhibited nonadapting firing rates ($ISI_L:ISI_F = 1.09 \pm 0.15$; $n = 101$) (see Materials and Methods) that ranged from 18 ± 13 Hz at rheobase (0.26 ± 0.09 nA) to 178 ± 38 Hz with higher current injections (Fig. 1*B*, right).

The connections between PC and FS cells were characterized by evoking action potentials in one cell and recording PSPs in the other (Fig. 1*C*). For the cells shown in Figure 1*A*, stimulation of the FS cell evoked IPSPs in both PC1 and PC2. Stimulation of the PC1, but not PC2, evoked EPSPs in the FS cell. Thus, PC1 is RC to the FS cell and PC2 is nRC through an inhibitory connection. This study focuses on the spatial distribution and properties of inhibitory connections in RC (red) versus nRC (blue) FS–PC pairs.

Variation of connection probability with intersomatic distance

We recorded a total of 315 FS–PC pairs and found 213 pairs had at least one synaptic connection between them. We calculated the probability of excitatory (P_E) and inhibitory (P_I) connections as well as RC (P_{RC}) and nRC (P_{nRC}) pairs as a function of intersomatic distance. We binned distance in 10–30 μm increments and, for each bin, estimated the probability of connection (P_C) by dividing number of connections (N_C) of a given type (C: E, I, RC, nRC) by the number of connections of that type tested (N_T). P_E decreased significantly between 20 μm (0.65 ± 0.08) and 100 μm (0.41 ± 0.08) (Fig. 2*A*) (*$p < 0.05$, Fisher's exact test), whereas P_I did not differ over the same range (0.55–0.47; $p > 0.10$).

Approximately 27% of FS–PC pairs were reciprocally connected ($n = 86$) (Fig. 2*B*, red triangles); the remaining connections were unidirectional (inhibitory: $n = 65$, blue triangles; excitatory: $n = 60$, black triangles; unconnected pairs are indicated by $+$ signs). The probability of inhibitory connections occurring in RC (P_{RC}) versus nRC (P_{nRCI}) FS–PC pairs also differed significantly with intersomatic distance. Within the ~40 μm radius of the FS cell, RC pairs outnumbered inhibitory nRCI pairs ~2:1 (Fig. 2*B*). Moreover, for distances <20 μm, the P_{RC} was nearly five times greater (0.45; red) (Fig. 2*C*) than the P_{nRCI} (0.10; blue; $p = 0.002$, Fisher's exact test). Between 20 and 50 μm, P_{RC} declined while the P_{nRCI} increased such that $P_{RC} \approx P_{nRCI} \approx 0.21$ at distances >50 μm. The probability of nonreciprocal excitatory connections (P_{nRCE}) over distance was comparable with P_{nRCI} (data not shown).

The spatial profile of RC pairs parallels that of excitatory connections—both P_{RC} and P_E decline by ~0.2 between 20 and 100 μm—suggesting that P_{RC} depends on P_E. It has been shown that
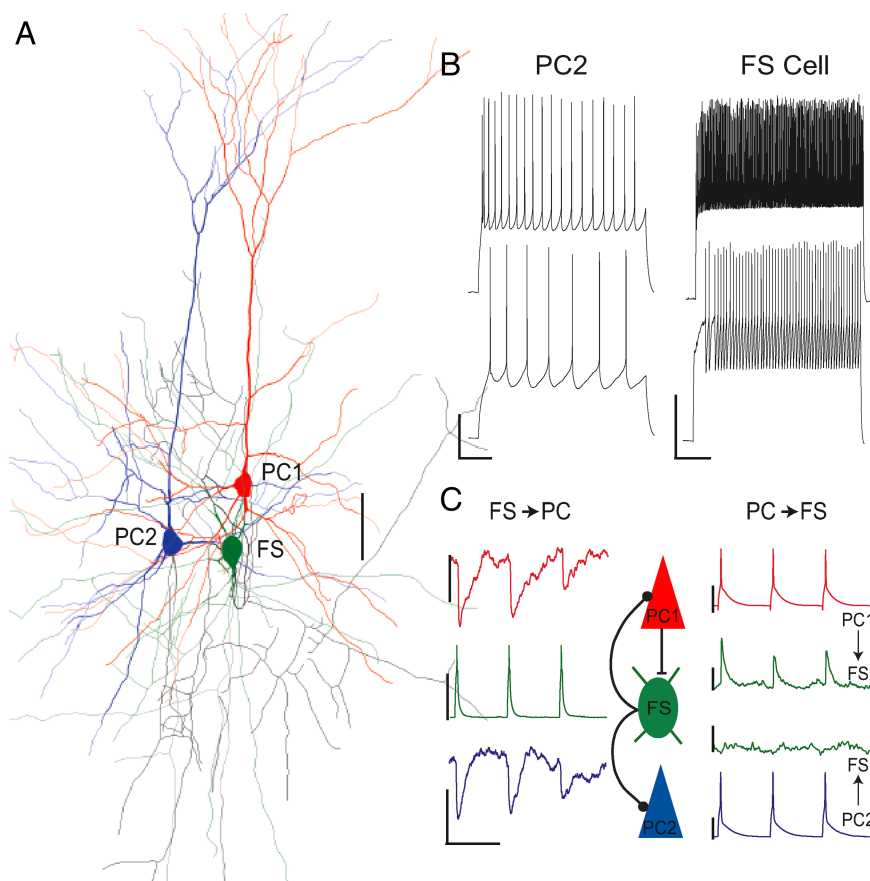

Figure 1. The intrinsic and synaptic properties of fast spiking interneurons and pyramidal cells. *A*, A representative FS cell (green) that was an RC pyramidal cell (PC1; red) and an nRC to another (PC2; blue). Scale bar, 50 μm. *B*, Responses evoked with depolarizing step current injection for the cells shown in *A* [left, PC2, 0.2 nA (bottom) and 0.4 nA (top); right, FS cell, 0.6 nA (bottom) and 0.8 nA (top)]. Calibration: vertical, 40 mV; horizontal, 200 ms. *C*, Left, Suprathreshold stimulation (10 Hz) of the FS cell (green trace) resulted in IPSPs in both PC1 (red trace) and PC2 (blue trace). Right, Stimulation of the RC PC1 (10 Hz; red trace) produced EPSPs in the FS cell (top; green trace). Stimulation of the nRC PC2 (blue trace) did not evoke EPSPs (bottom; green trace). Calibration: vertical, PSPs, 0.5 mV; action potentials, 40 mV; horizontal, 100 ms.

presence of a reciprocal connection can be predicted based on excitatory connectivity in primary visual cortex (V1) (Yoshimura and Callaway, 2005). We performed similar analyses and found that because of the high, nearly equal numbers of excitatory ($n = 151$) and inhibitory ($n = 146$) connections, the number of reciprocal connections ($n = 86$) depended equivalently on P_E and P_I ($p = 0.04$, Fisher's exact test). Thus, in contrast to V1, there is an equal likelihood of finding an RC pair when either an excitatory or inhibitory connection is found. In V1, P_E is much lower (0.19) than ACx, whereas P_I (~0.47) is comparable in both areas (Yoshimura and Callaway, 2005). This difference may underlie the dependence of RC pairs on excitatory connection in V1. The differences in P_E between V1 and ACx were not attributable to differences in postnatal day age of the animals used in the two studies [P21–P26 (Yoshimura and Callaway, 2005) vs P14–P29 in the present study]. We found that the P_I (~0.45) does not vary with age, whereas P_E increased slightly from ~0.40 between P14 and P18 to ~0.55 at P19–P29 (supplemental Fig. 1*A*, available at www.jneurosci.org as supplemental material). Thus, these results may reflect differences in the connection architecture of V1 versus ACx rather than the age of the animal.

We further investigated whether or not reciprocal connections occurred with greater probability than predicted if excitatory and inhibitory connections occur independently. When P_E
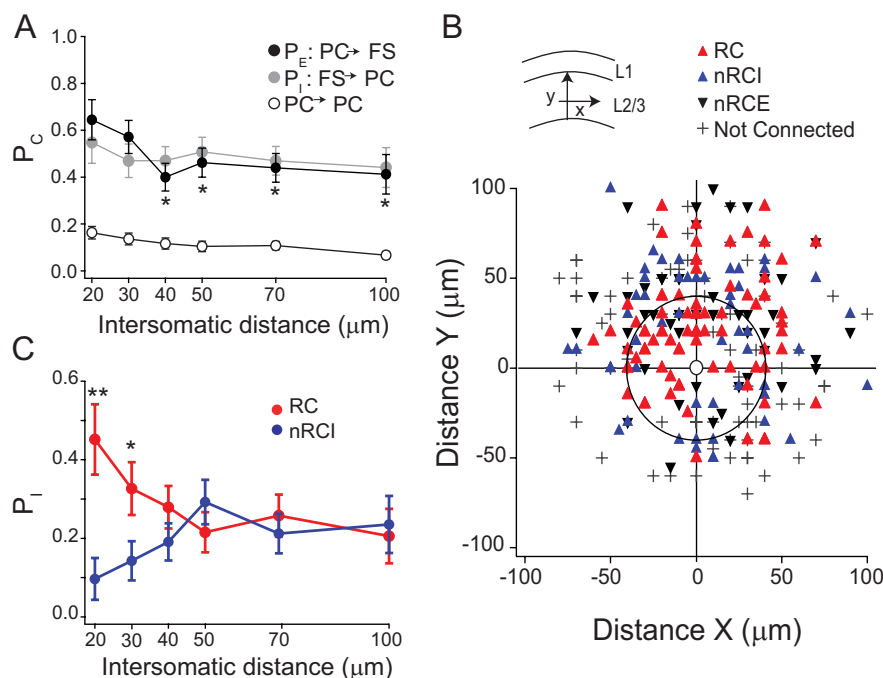
Figure 2. Variation in connection probability with distance. **A**, The probabilities of excitatory (P_E; black circles) and inhibitory (P_I; gray circles) connections between FS–PC pairs and between PC–PC pairs (open circles) [from Oswald and Reyes (2008)] are plotted against the intersomatic distance. The P_E at 20 μm was significantly different from that at 40, 50, 70, or 100 μm (*$p <$ 0.05, Fisher's exact test). P_I was not significantly different at any distance. **B**, The relative horizontal (x) and vertical (y) locations of PCs that were reciprocally (red triangles) or nonreciprocally connected through an inhibitory (FS to PC; nRCI; blue triangles) or excitatory (PC to FS; nRCE; inverted black triangles) synapse to FS cells (open circle) aligned to the origin. Unconnected PCs are indicated with "+" signs. The circle denotes the 40 μm region around the FS cell. Inset, Schematic of the slice orientation with L1 at the top of the field of view and x–y positions in L2/3. **C**, The probability of inhibitory connections occurring in RC (red) or nRCI (blue) FS–PC pairs plotted against intersomatic distance. The P_{RC} was significantly greater than P_{nRCI} between nearby neurons [**$p = 0.002$ (20 μm), *$p = 0.03$ (30 μm), Fisher's exact test]. Error bars are as follows: $SE_p = (P_c(1 - P_c)/N_T)^{1/2}$, where P_c is the connection probability and N_T is the number of pairs sampled (see Materials and Methods).

Table 1. Recorded and predicted probability of connection with intersomatic distance

Distance (μm)	P_{RC}			P_{nRCI}		
	Recorded	Predicted	p value	Recorded	Predicted	p value
20	0.45	0.35	0.61	0.1	0.18	0.47
30	0.32	0.27	0.65	0.14	0.2	0.59
40	0.28	0.18	0.31	0.19	0.28	0.31
50	0.21	0.23	1	0.23	0.27	1
70	0.24	0.18	0.68	0.21	0.26	0.68
100	0.20	0.18	1	0.18	0.26	1
<50	0.30	0.24	0.23	0.20	0.24	0.29

The recorded P_{RC} and P_{nRCI} and predicted, $P_{RC}(d) = P_E(d)P_I(d)$ and $P_{nRCI}(d) = P_I(d)(1 - P_E(d))$, did not differ at any distance (values of $p > 0.05$, two-tailed, Fisher's exact test). Recorded and predicted values also did not differ when connections <50 μm were pooled (values of $p > 0.05$, two-tailed, Fisher's exact test).

and P_I vary with distance, d, the predicted $P_{RC}(d) = P_E(d)P_I(d)$ and $P_{nRCI}(d) = P_I(d)(1 - P_E(d))$, assuming independent connectivity is comparable with recorded values at all distances (Table 1) ($p = 0.31–1$, Fisher's exact test). This result is not an artifact of bin size: when all connections <50 μm were pooled, the recorded and predicted probabilities did not significantly differ (Table 1). In summary, the high P_{RC} between FS–PC pairs separated by <50 μm follows the spatial profile of excitatory connections but is otherwise consistent with the hypothesis that PC to FS and FS to PC connections occur independently.

The differences in the spatial profile of P_E and P_I are not likely attributable to cutting artifacts. Although a recent anatomical study has suggested that estimates of long-range (>200 μm) ex-

citatory connectivity are more susceptible to slicing artifacts than inhibitory connectivity (Stepanyants et al., 2009), the present study focuses on neurons separated by <100 μm. In addition, excitatory connectivity has been shown to be constant between 0 and 50 μm below the slice surface (Song et al., 2005), and the majority of our neurons were located at least 40 μm below the surface. Finally, in biocytin-filled neurons, we saw minimal evidence of truncation (blebs) within the 100 μm region around the recorded neurons.

The geometry of neuronal arbors could underlie the differences in the spatial profiles of excitatory versus inhibitory connections. The dendritic and axonal arbors of a PC (Fig. 1) and FS cell (Dumitriu et al., 2007) would be expected to overlap extensively within 100 μm (Stepanyants et al., 2008). However, PC axons initially descend toward L5 and send collaterals to L2/3, whereas FS axons tend to be more symmetrical. This difference could result in a nonuniform profile in excitatory connectivity. We ascertained the distributions of excitatory and inhibitory connections given the relative positions of the presynaptic and postsynaptic cell within the x–y plane of the slice (supplemental Fig. 1B–D, available at www.jneurosci. org as supplemental material). Excitatory connections were more probable (0.52 ± 0.04) when the PC was superficial (closer to L1) to the FS cell than vice versa (0.32 ± 0.06; $p = 0.003$, Fisher's exact test). The probability of inhibitory connection did not differ with respect to the presynaptic FS cell ($p = 0.10$, Fisher's exact test). This suggests that the decline in P_E could, in part, be attributed to decreased overlap between the vertically descending PC axon and the dendrites of the FS cell.

Inhibitory synaptic responses

To compare the inhibitory synaptic responses of RC and nRC pairs, we performed simultaneous current-clamp recordings from a triplet consisting of a single FS cell that was reciprocally connected to one PC and unidirectionally connected to a second PC ($n = 19$) (Fig. 3A, inset). The FS cell was driven to fire action potentials at 80 Hz for 500 ms (40 pulses) while the evoked inhibitory responses were recorded in the two PCs. Both PCs received constant current injections to maintain similar holding potentials (RC, −61 ± 4 mV; nRC, −62 ± 4 mV).

In RC and nRC PCs, the IPSPs summated to produce a transient onset hyperpolarization that settled to a steady-state value (Fig. 3A). The inhibitory response returned to baseline within 500 ms of stimulus offset. The amplitudes of the first IPSPs of the trains ($IPSP_1$) were comparable in RC (0.7 ± 0.4 mV) and nRC (0.7 ± 0.5 mV; $p = 0.95$, paired t test; $n = 19$) pairs. However, for any given triplet, the strengths of $IPSP_1$ in RC versus nRC pairs often differed in a nonsystematic manner. To correct for this variation and allow for direct comparisons between nRC and RC pairs, all ensuing measures of inhibitory strength are computed

relative to $IPSP_1$. The steady-state hyperpolarization (H_{SS}) was taken as the average membrane voltage in the last 200 ms of stimulation (Fig. 3B). The relative increase in inhibition during stimulation, H_{SS}-$IPSP_1$, was significantly greater in nRC versus RC pairs both within triplets (nRC, 0.5 ± 0.4 mV; RC, 0.2 ± 0.3 mV; $p = 0.03$; $n = 19$; paired t test) and over all pairs [nRC ($n = 22$), 0.4 ± 0.3 mV; RC ($n = 26$), 0.1 ± 0.3 mV; $p = 0.008$, unpaired t test] (Fig. 3B). We measured the area (millivolts · milliseconds) of the postsynaptic response to 80 Hz stimulation normalized by the area (millivolts · milliseconds) of an IPSP elicited by a single pulse (Thomson et al., 1996) (Fig. 3A, inset). The normalized inhibitory area of RC pairs was significantly less than nRC pairs over all recordings (RC, 18 ± 7, $n = 26$; nRC, 24 ± 9, $n = 22$; $p = 0.013$), as well as in the triple neuron recordings (RC, 18 ± 8; nRC, 25 ± 12; $p = 0.007$; $n = 19$) (Fig. 3C,D).

The difference in inhibition between RC and nRC pairs was not attributable to the properties of the PC or FS cells. Within the triplets, PCs shared the same FS cell and had similar membrane time constants (RC, 23 ± 10 ms; nRC, 18 ± 10 ms; $p = 0.3$) and input resistances (RC, 175 ± 63 MΩ; nRC, 161 ± 68 MΩ; $p = 0.6$). The inhibitory synapses within RC and nRC pairs show comparable short-term depression (see Materials and Methods) during 80 Hz stimulation of the FS cell (Fig. 4A) and no long-term changes in synaptic responses (data not shown). Finally, ratio of the total inhibitory areas in nRC pairs versus RC pairs did not vary with age (nRC:RC at P14–P18: 1.30 ± 0.17, $n = 7$; P19–P29: 1.36 ± 0.35, $n = 12$; $p > 0.05$).

The differences in inhibition between RC and nRC pairs were attributable to differential $GABA_B$ receptor activation. The isolated $GABA_B$ portion of the response was first inferred and then verified pharmacologically in the following manner. The IPSP evoked with a single action potential is mediated primarily by $GABA_A$ currents (Connors et al., 1988) and can be used as a template for $GABA_A$ receptor activation (Fig. 4B, middle). For each stimulus pulse of the train, this template was scaled by the measured short-term synaptic depression (Fig. 4B, top). The linear superposition of all the waveforms gave the predicted $GABA_A$ portion of the response (Fig. 4B, middle, gray line). Subtraction of the predicted $GABA_A$ component from the total recorded response (Fig. 4B, bottom, gray line) yielded the predicted $GABA_B$ component. In a subset of triple neuron recordings ($n = 8$), we blocked the $GABA_A$ component with bath application of 10 μM bicuculline. The remaining inhibitory response was small (0.1–0.8 mV) and had a delayed onset consistent with $GABA_B$-mediated responses (Connors et al., 1988) (Fig. 4B, bottom, blue line). The area of the recorded $GABA_B$ components did not differ from the predicted area values ($p = 0.10$, Wilcoxon's rank test). The $GABA_B$ receptor antagonist, 2-hydroxysaclofen (50 μM),
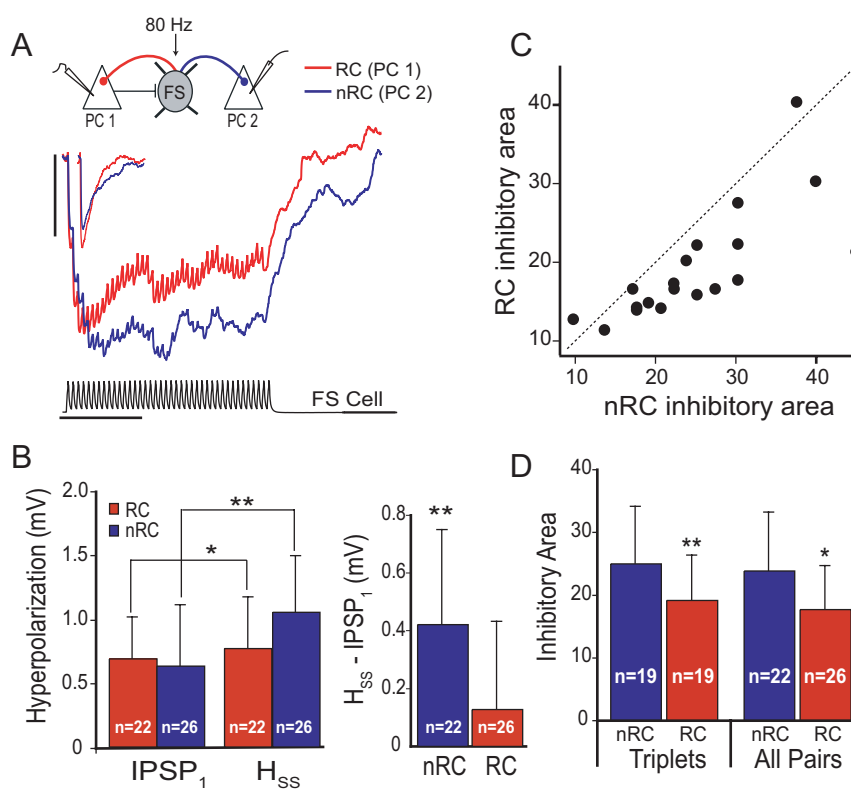

Figure 3. Inhibitory synaptic responses in RC and nRC pairs. **A**, Postsynaptic responses (average of 15 trials) evoked simultaneously (inset shows a schematic of triple recording) in RC (red) and nRC (blue) connected PCs during 80 Hz stimulation of the presynaptic FS cell. Calibration: vertical, FS cell, 40 mV; PCs, 1 mV; horizontal, 200 ms. **B**, Left, Over all pairs, the amplitudes of the first IPSP ($IPSP_1$) of the train did not significantly differ in RC (0.7 ± 0.3 mV; $n = 26$) versus nRC (0.6 ± 0.5; $n = 22$; $p = 0.77$, unpaired t test) pairs. In both RC (red; *$p = 0.012$) and nRC (blue; **$p = 5 \times 10^{-6}$) pairs, the steady-state hyperpolarization (H_{SS}) recorded during the last 200 ms of stimulation was greater than the amplitude of $IPSP_1$. Right, The increase in inhibition during stimulation, H_{SS}-$IPSP_1$, is significantly greater in nRC versus RC pairs (**$p = 0.008$, unpaired t test). **C**, The inhibitory area normalized by the area of a single IPSP (**A**, inset) in the RC PC is plotted versus that of the nRC PC for each triple neuron recording ($n = 19$; black circles). In nearly all triplets, inhibitory area in the nRC pair was greater than the RC pair (i.e., below the dashed unitary slope line). **D**, The average inhibitory area was significantly greater in nRC pairs versus RC pairs in triplets (left; **$p = 0.007$, paired t test) and over all pairs (right; *$p = 0.013$, unpaired t test).

blocked the remaining inhibitory component ($n = 4$ pairs) (Fig. 4C; supplemental Fig. 2A, available at www.jneurosci.org as supplemental material).

As observed for the total synaptic response (Fig. 3), the recorded steady-state $GABA_B$ component was smaller in RC (0.2 ± 0.1 mV) versus nRC pairs (0.4 ± 0.2 mV; $p = 0.02$, Wilcoxon's rank test; $n = 8$). For the majority of triplets, the predicted (filled circles) and recorded (open circles) area of the $GABA_B$ component in the RC pair was less than that of the nRC pair (Fig. 4D). On average, the area of the $GABA_B$ component in nRC pairs was ~2.5 times greater (range, 1–9) than in RC pairs (Fig. 4E) (predicted area: triplets: RC, 7 ± 5; nRC, 16 ± 9, $p = 0.009$; full dataset: RC, 6 ± 4; nRC, 16 ± 9, $p = 0.00003$; recorded area: RC, 5 ± 4; nRC, 12 ± 9, $p = 0.025$). Finally, for each triplet, the difference in total area between RC and nRC pairs was linearly correlated with the difference in the predicted $GABA_B$ in the same pairs ($r = 0.66$; slope, 0.98 ± 0.27; $p = 0.002$) (Fig. 4F).

In summary, we have shown that both the spatial profiles and the $GABA_B$ receptor-mediated responses differ in RC and nRC pairs. This implies that nearby neurons have a high P_{RC} and likely receive less $GABA_B$-mediated inhibition. As P_{nRCI} increases with intersomatic distance, so does the recruitment of $GABA_B$-mediated responses. Overall, this suggests a spatial profile for inhibition. The amplitudes of unitary IPSPs did not
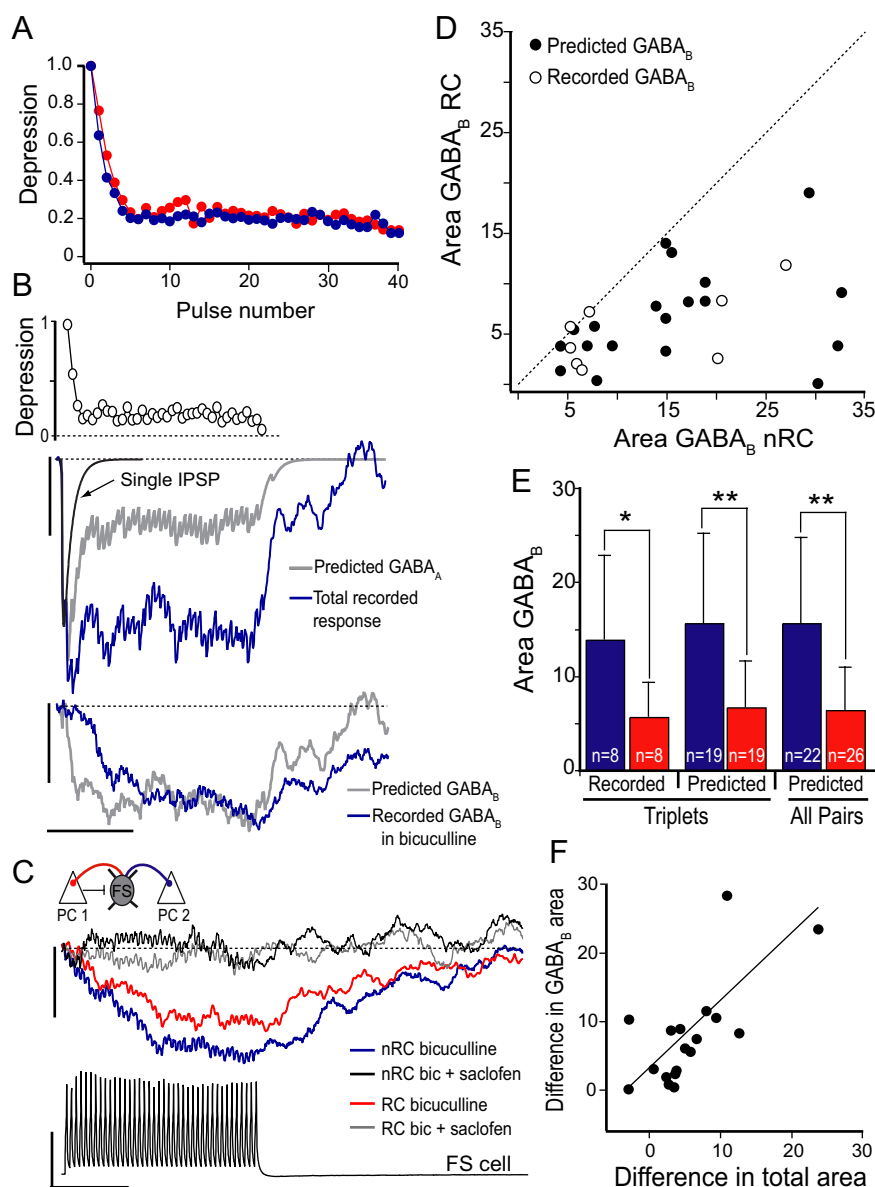
Figure 4. GABA$_B$-mediated inhibition is stronger in nRC versus RC pairs. **A**, The mean short-term synaptic depression of successive IPSPs normalized by the amplitude of first IPSP in RC (red; $n = 19$) and nRC (blue; $n = 19$) PCs during 80 Hz stimulation (40 pulses) of the FS cell. Error bars were omitted for clarity. **B**, Top, The short-term depression (open circles) of the total inhibitory response (blue trace; middle) of an nRC pair. Middle, The predicted GABA$_A$ (gray trace) component of the inhibitory response obtained by convolving 40 pulses (80 Hz pulse rate) with the template IPSP (black trace) scaled by the measured short-term depression (above). Bottom, The predicted GABA$_B$ component (gray trace) was obtained by subtracting the predicted GABA$_A$ component from the total inhibitory response. The isolated GABA$_B$ component (blue trace) recorded in the presence of 10 μM bicuculline is shown for comparison. **C**, The isolated GABA$_B$ components in RC (red) and nRC (blue) PCs recorded in 10 μM bicuculline during 80 Hz firing of the FS cell (black trace). In both PCs, this response was abolished by bicuculline plus 50 μM saclofen (RC, gray trace; nRC, black trace). **D**, For all triplets, the area of the predicted (filled circles) and recorded (open circles) GABA$_B$ response in the nRC PC was plotted versus that of the RC PC. All points were on or below the unit line (dashed line). These areas were normalized by the area of the first IPSP for comparison with Figure 3C. **E**, The average area of the GABA$_B$ component in RC pairs (red) was significantly smaller than in nRC pairs (blue) (recorded GABA$_B$, *$p = 0.025$, Wilcoxon's rank test; predicted GABA$_B$, triplets, **$p = 0.009$, paired t test; all pairs, **$p = 0.00003$, unpaired t test). The area of the recorded GABA$_B$ in both RC and nRC pairs did not significantly differ from predicted GABA$_B$ responses ($p = 0.10$, Wilcoxon's rank test). **F**, The difference in the predicted GABA$_B$ areas between nRC and RC pairs was correlated with the difference in total area (Fig. 3C) for the same pairs ($R = 0.66$; slope, 0.98 ± 0.27; $p = 0.002$). Calibration: vertical, PC, 0.2 mV; FS, 40 mV; horizontal, 200 ms.

differ between RC and nRC pairs and did not vary with intersomatic distance (supplemental Fig. 2B, available at www.jneurosci.org as supplemental material). However, there was a trend toward increasing GABA$_B$ responses with intersomatic distance (supplemental Fig. 2C, available at www.jneurosci.org as supplemental

material). Unfortunately, there were insufficient data in each distance bin for statistical analysis of these results.

Model of L2/3 FS–PC circuitry
The functional implications of the experimental findings were explored with a network model that incorporated key aspects of the measured FS–PC circuitry and synaptic properties (see Materials and Methods). In brief, the network was a 150×150 μm sheet of 900 PCs and 225 FS cells, in which each cell was modeled as a leaky integrate-and-fire neuron. The probability of a PC to PC connection was 0.1 and spatially independent (Fig. 5A, black). The connection probability between PC and FS cells depended on the intersomatic distance such that at distances <50 μm, P_{RC} was high and P_{nRCl} was low (Fig. 5A). The GABA$_A$ conductances were equivalent in RC and nRC pairs, whereas the GABA$_B$ conductance was three times greater in nRC pairs (Fig. 5B, left). The membrane potential responses of an RC or nRC PC to an FS cell that fired action potentials at 80 Hz for 500 ms are shown in Figure 5B, right. These parameters produced a $H_{SS,nRC}/H_{SS,RC}$ ratio ($\sim$2.2) in model PCs that was within the range of recorded $H_{SS,nRC}/H_{SS,RC}$ ratios (2.4 ± 2.8) (supplemental Fig. 3, available at www.jneurosci.org as supplemental material).

Exactly 64 PC and 16 FS cells were chosen at random within a square region of length, L, positioned at the center of the network (Fig. 5C, yellow cells). These cells were driven (D) with a high rate excitatory Poisson input; all other cells were not driven (ND), and received a weak background excitatory input (Fig. 5C, gray cells). Therefore, the network consisted of driven/nondriven PCs (PC$_D$, PC$_{ND}$), and driven/nondriven FS cells (FS$_D$, FS$_{ND}$). Sample membrane traces for driven and nondriven cells are shown in Figure 5D. Note that neurons in the PC$_{ND}$ population were suppressed by recurrent FS cell activity (Fig. 5D) and did not contribute to network dynamics (data not shown).

The spatial profile of inputs modulate gamma oscillations
The combination of the RC and nRC spatial connectivity profile and the differential recruitment of GABA$_B$ in these microcircuits suggest that the network response can be modulated by the spatial profile of input (Fig. 6A). Spatially focal inputs ($L = 40$ μm) produced a synchronous PC$_D$ cell response (Fig. 6B, top) that oscillated strongly at gamma frequencies ($\sim$40 Hz), as evidenced by the large peak in the power spectrum of the PC$_D$ population (Fig. 6C, top). An increase in L

decreased both the degree of PC_D synchrony (Fig. 6 B, middle and bottom) and the power of the network gamma oscillation (Fig. 6 C, middle and bottom). The change in power, quantified by the Q factor (height/width of the gamma peak) (Fig. 6 D, inset), decreased dramatically as L increased from 40 to 150 μm (Fig. 6 D). The strong gamma oscillation at L = 40 μm was robust to perturbations in the synaptic weights (supplemental Fig. 3, available at www.jneurosci.org as supplemental material) and input strength (data not shown).

Gamma oscillations in the PC_D, FS_D, and FS_{ND} subnetworks

The above results raised two related questions. First, how do neural interactions within the model network generate gamma oscillation? And, second, why is the gamma band oscillatory power influenced by L? To determine the mechanisms that underlie gamma oscillations and the dependence on L, we examined the subnetwork interactions among the PC_D, FS_D, and FS_{ND} populations (Fig. 7 A).

The dependence of gamma oscillations on L (Fig. 6 D) was not simply a result of a change in overall network activity. The heterogeneity in network connectivity produced a large spread in the firing rate distributions (Fig. 7 B). Changes in L did not significantly influence these firing rates (Fig. 7 B) because the relatively small difference in inhibitory strength between nRC and RC pairs was insufficient to suppress firing in the PC network.

Although changing L did not affect the average firing rate, the temporal patterning in the network activity was altered substantially. At L = 40 μm, the spike train raster plots of the PC_D and FS_{ND} cells showed significant banding and the instantaneous population firing rates had large-amplitude, rhythmic fluctuations (Fig. 7 C, top and bottom). In contrast, the cells in FS_D population were asynchronous, and the population firing rates had small-amplitude, aperiodic fluctuations (Fig. 7 C, middle). The power spectrums of the PC_D and FS_{ND}, but not the FS_D, population responses had a significant peak in the gamma frequency band (~40 Hz) (Fig. 7 D, black). The PC_D network oscillation reflected synchronous activity among the PC_D neurons as indicated by the high coherence between the spike trains of individual PC_D pairs (Fig. 7 D, left, inset). The PC_D and FS_{ND} population oscillations were anticorrelated (Fig. 7 E, middle, black) with a phase shift of ~90° (data not shown). Both the PC_D and FS_{ND} populations were weakly correlated with the FS_D population (Fig. 7 E, left and right, black curves). Finally, the oscillatory power in all populations was reduced for L = 150 μm compared with L = 40 (Fig. 7 C–E, compare green and black curves).

$GABA_B$ recruitment modulates gamma oscillations

Consistent with previous findings (Brunel and Wang, 2003; Börgers et al., 2005; Börgers and Kopell, 2005), the anticorrelated PC_D and FS_{ND} populations (Fig. 7 E, middle) gave rise to gamma rhythms. Synchronous input from the PC_D population drove activity in the FS_{ND} population (Fig. 8 A, right, black line). After a short delay associated with synaptic recruitment, the recurrent
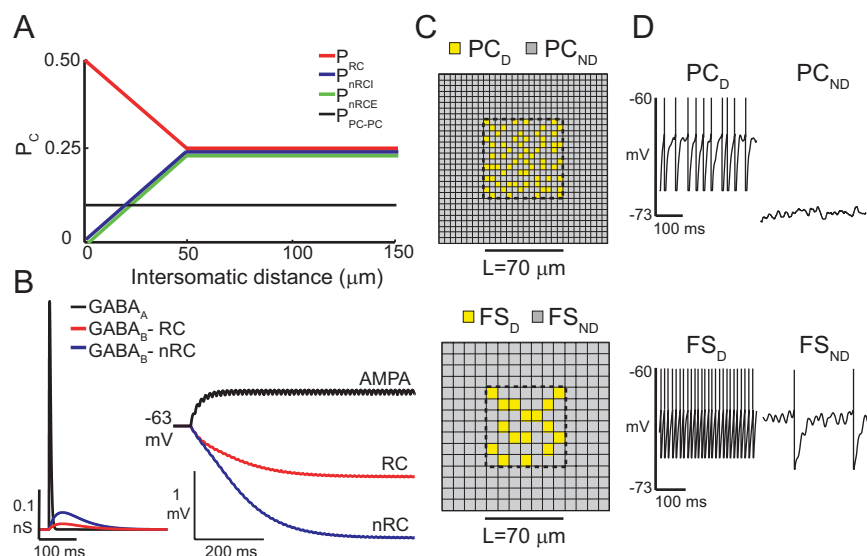
Figure 5. Model L2/3 network. **A**, Probability of connection (P_c) as a function of intersomatic distance. The spatial connectivity profiles of PC–FS pairs: P_{RC} (red), P_{nRCI} (blue), P_{nRCE} (green), as well as $P_{PC–PC}$ (black) qualitatively matched the experimental data (Fig. 2C). **B**, Left, Conductance for a single inhibitory synaptic event in a PC decomposed into the $GABA_A$ (black), and $GABA_B$ for the RC (red) and nRC (blue) connection. Right, Membrane potential responses when a presynaptic PC (excitatory synapse; black) or FS cell [mixed $GABA_A/GABA_B$ inhibitory synapse for RC (red) and nRC (blue)] fired action potentials at 80 Hz for 500 ms. **C**, Left, Spatial profile of input to PC and FS populations: driven cells (D) are shown in yellow, and nondriven (ND) cells are gray. The cells are located on grid points. The size of the stimulus region is given by box of side length L (i.e., L = 70 μm; dashed line). **D**, Sample V_m trace for a cell of each class: PC_D, PC_{ND}, FS_D, and FS_{ND}.

inhibition from the FS_{ND} population (Fig. 8 A, right, gray line) decreased PC_D activity. The subsequent drive to FS_{ND} neurons was in turn reduced. This decreased feedback inhibition from the FS_{ND} population, allowing the PC_D population to resume firing, and repeat the cycle. In contrast, the activity of the FS_D population was dependent on external drive and was weakly influenced by PC_D activity (Fig. 7 E, left). The high firing rates of the FS_D interneurons (~80 Hz) (Fig. 7 B, middle) prevented entrainment of these cells to the gamma cycle (Börgers and Kopell, 2005). Consequently, the FS_D population acted primarily as a source of feedforward inhibition to the PC_D and PC_{ND} populations (Fig. 8 B). The sensitivity of the network oscillation to L was qualitatively robust to FS_D firing rates of ~40–200 Hz (supplemental Fig. 4, available at www.jneurosci.org as supplemental material).

The strength of the FS_D feedfoward inhibition depended on L and provided the basis for spatial control of network oscillations. This can be seen by overlaying the P_{RC} and P_{nRCI} with the probability density (pd) of the intersomatic distances of driven FS–PC pairs for L = 40 and L = 150 μm (Fig. 8 B, left). When L = 40 μm, most of the driven PC_D–FS_D pairs (the mass of pd) were separated by distances in the 0–50 μm region dominated by RC pairs (gray), and thus, the majority were reciprocally connected. For L = 150 μm, the pd of intersomatic distances decreased in the 0–50 μm range and extended to 150 μm (green). Consequently, the number of RC and nRC PC_D–FS_D pairs was nearly equal. Therefore, the high number of RC pairs driven at L = 40 μm, combined with the weak recruitment of $GABA_B$-mediated inhibition in RC pairs, resulted in minimal feedfoward $GABA_B$ to any given PC_D (Fig. 8 B, right, closed circles). As L increased, the decrease in the number of RC pairs coupled with the increase in nRC pairs increased the overall level of $GABA_B$ (Fig. 8 B, right). This in turn suppressed synchronous PC_D discharge, and reduced the recruitment of the FS_{ND} population, and ultimately, attenuated gamma activity in the recurrent PC_D/FS_{ND} subnetwork.
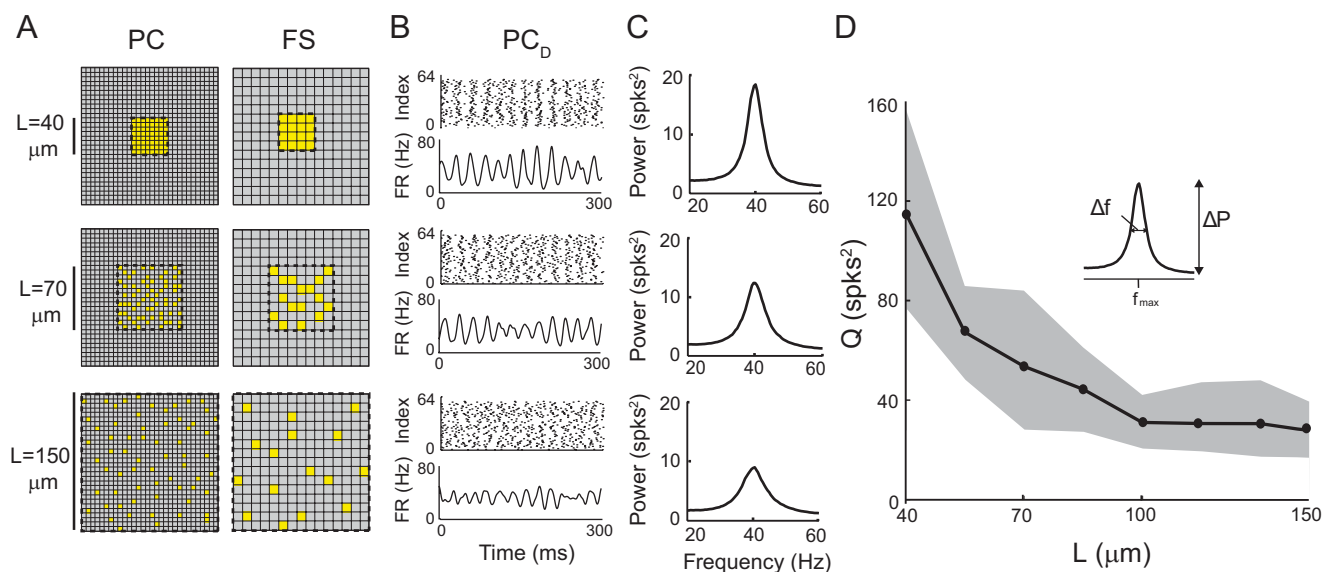
Figure 6. Spatial extent of input modulates gamma activity in driven PCs. ***A***, Driven neurons [$n = 64$ PCs (PC$_D$) and $n = 16$ FS cells (FS$_D$)] were chosen randomly from a square area of length L centered in the middle of the network. Simulation results for three lengths are shown: $L = 40$, 70, and 150 μm. ***B***, Spike train raster plots and instantaneous firing rates for PC$_D$ for the three values of L. Instantaneous firing rates were computed by convolving the network spike train, $Y_{\alpha,\beta}(t)$ (α = PC, FS; β = D, ND), with a Gaussian kernel with a SD of 2 ms. ***C***, Normalized power spectrum of the PC$_D$ population for the three values of L. The curves are averages computed from 120 realizations in which the network connectivity and chosen driven cells were randomized. ***D***, The Q factor ($Q = f_{max}\Delta P/\Delta f$) plotted against L. The gray region denotes ± 1 SD computed across 120 realizations.

Since a large proportion of FS$_{ND}$ cells were nonreciprocally connected to the PC$_D$ population, they also provided significant GABA$_B$ inhibition. However, the recruitment of this inhibition was insensitive to changes in L because the majority of FS$_{ND}$–PC$_D$ connections occur between neurons separated by >50 μm. Last, since the strength of GABA$_A$ did not differ between RC and nRC pairs, the recruitment of GABA$_A$ was independent of L (Fig. 8B, right, open circles) and thus did not contribute to the modulation of oscillatory activity.

To verify that L-dependent recruitment of GABA$_B$ modulates of gamma oscillations, we applied a constant GABA$_B$ conductance (H) to the PC$_D$ population when $L = 40$ μm (Fig. 8C, left). The strong gamma oscillation for $H = 0$ nS (black dashed line) decreased when $H = 1.2$ nS (cyan line) and matched the weak oscillatory power when $L = 150$ μm and $H = 0$ nS (green line) (Fig. 8C, middle). The decrease in gamma power with H was gradual, indicated by the shallow decline of the Q factor (Fig. 8C, right). Similar results were obtained in the hippocampus in which synaptic activation of GABA$_B$ receptors decreased the entrainment of neurons and power of gamma oscillations (Brown et al., 2007).

To explore the influence of the spatial profile of network connectivity on gamma oscillations, we (1) replaced the spatially dependent probability distributions of RC and nRC pairs with flat, spatially independent distributions (Fig. 8D) and (2) equalized the strength of GABA$_B$-mediated inhibition in RC and nRC pairs (Fig. 8E). In both cases, the influence of spatial profile of the input (L) on the network oscillation was abolished. The first manipulation removed all spatial structure from the network, thereby making it impossible for the network to be sensitive to the spatial profile of inputs. The second manipulation maintained the spatial profile of RC versus nRC connections, but the lack of differential GABA$_B$-mediated responses resulted in an inhibitory field that was insensitive to the spatial profile of inputs. In summary, it is the combination of the spatial profiling of RC and nRC connections and the differential GABA$_B$ across these two circuits that allowed the spatial distribution of excitatory drive to modulate gamma oscillatory activity throughout the model ACx network.

Discussion

In the present study, inhibitory connections between nearby (<50 μm) PC and FS cells in ACx occurred predominantly in RC pairs, whereas at greater intersomatic distances (50–100 μm) RC and nRC pairs were equally probable. Furthermore, GABA$_B$-mediated inhibition was weaker in RC than nRC pairs. Combined, these results suggest that PCs within ~ 50 μm of a connected FS cell receive less steady-state hyperpolarization during network activity. A network model incorporating this experimental data showed that spatially focal inputs elicit strong, synchronous, network gamma oscillations. Conversely, spatially broad inputs recruited more GABA$_B$-mediated inhibition that suppressed gamma band activity. These findings demonstrate that the connectivity and recruitment of inhibition within FS–PC circuits allow the spatial profile of inputs to L2/3 to modulate gamma oscillations in ACx.

PC and FS cell connectivity

The probability of connection between L2/3 PC–FS pairs in ACx was high (~ 0.5) compared with the connectivity between PC–PC pairs (~ 0.11) (Oswald and Reyes, 2008). Reciprocal connected FS–PC pairs were also highly probable (up to 0.45). Similar results have been reported in other cortical areas (Holmgren et al., 2003; Thomson and Lamy, 2007). Both P_E and P_{RC} decreased significantly with intersomatic distance between 20 and 100 μm. Since P_I did not vary with distance, it appeared that P_{RC} depended on P_E rather than P_I. However, the recorded P_{RC} was consistent with the hypothesis that excitatory and inhibitory connections in RC pairs occur independently, albeit with different spatial profiles. We propose that the spatial profile of P_E, and subsequently P_{RC}, arises because of the anatomical structure and orientation of PC and FS cells. In contrast, the P_E between FS–PC pairs in V1 is much lower and the presence of excitatory connections is predictive of RC pairs (Yoshimura and Callaway, 2005). The differences
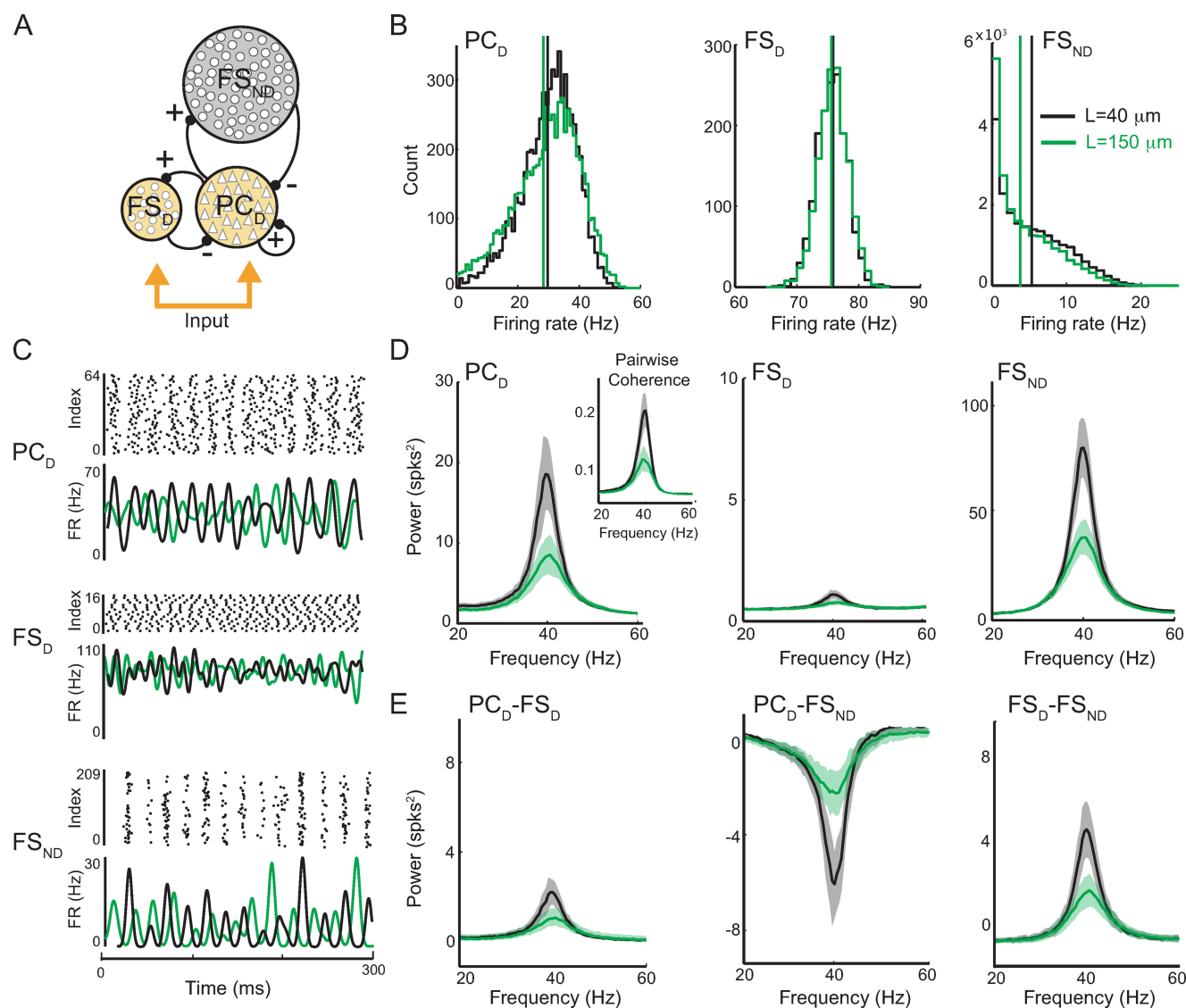
Figure 7. Spike train patterning in PC_D, FS_D, and FS_{ND} subnetworks. **A**, Schematic of the L2/3 network showing the PC_D, FS_D, FS_{ND} subnetworks and their interactions. **B**, Distribution of time averaged firing rates for the PC_D (left), FS_D (middle), and FS_{ND} (right) computed from 120 network realizations. The ensemble average firing rate is shown as a vertical line. The network with input $L = 40$ μm (black) and $L = 150$ μm (green) have the same firing rate. **C**, Spike train raster plots and instantaneous firing rates for the PC_D (top), FS_D (middle), and FS_{ND} (bottom) networks. The spike raster plots are for the network with $L = 40$ μm, whereas the firing rates are sample realizations of the network with stimulus region over $L = 40$ μm (black) and $L = 150$ μm (green). **D**, Normalized power spectra for PC_D (left), FS_D (middle), and FS_{ND} (right) (colors as in **C**). **E**, Normalized cross spectra between the PC_D–FS_D (left), PC_D–FS_{ND} (middle), and FS_D–FS_{ND} (right) subnetworks (colors as in **C**). Only the value of the real component is plotted. In **D** and **E**, shaded areas indicate ±1 SD computed across 120 realizations in which the network connectivity and chosen driven cells were randomized.

in P_E and P_{RC} between V1 and ACx were not attributable to the postnatal day age and may reflect regional differences in connectivity.

In the present study, connections (chemical or electrical) between FS cells were not examined. It has been suggested that these connections enhance synchrony among FS cells and promote gamma oscillations (Hormuzdi et al., 2001; Brunel and Wang, 2003; Börgers and Kopell, 2005). Inclusion of FS–FS interactions in our model would likely increase gamma band oscillatory synchrony between FS_D cells. However, the slow time course of $GABA_B$ (approximately hundreds of milliseconds) compared with gamma frequencies would continue to suppress oscillatory responses to spatially broad inputs. Thus, we expect that FS–FS interactions would not qualitatively alter the sensitivity of gamma oscillations to the spatial scale of input, unless the spatial profile of these connections differs from PC–FS interactions.

Differential $GABA_B$-mediated inhibition

The $GABA_B$-mediated inhibitory responses were stronger in nRC than RC pairs. Although this difference was small for individual pairs (0.1–0.6 mV), the accumulation of $GABA_B$ inhibition during population activity can significantly impact neural processing. For example, stimulation of neural populations in ACx produces ~5 mV $GABA_B$-mediated potentials in PCs (Buonomano and Merzenich, 1998). Using a network model, we assessed the functional implications of the recorded connectivity and synaptic parameters at the population level. The model accounted for the relative weakness of the differential synaptic responses in that increased recruitment of $GABA_B$ with spatially broad stimulation did not influence neural firing rates (Fig. 7B). Nevertheless, the differential $GABA_B$-mediated response was sufficient for the spatial extent of input to significantly modulate network oscillations. This is consistent with the fact that weak
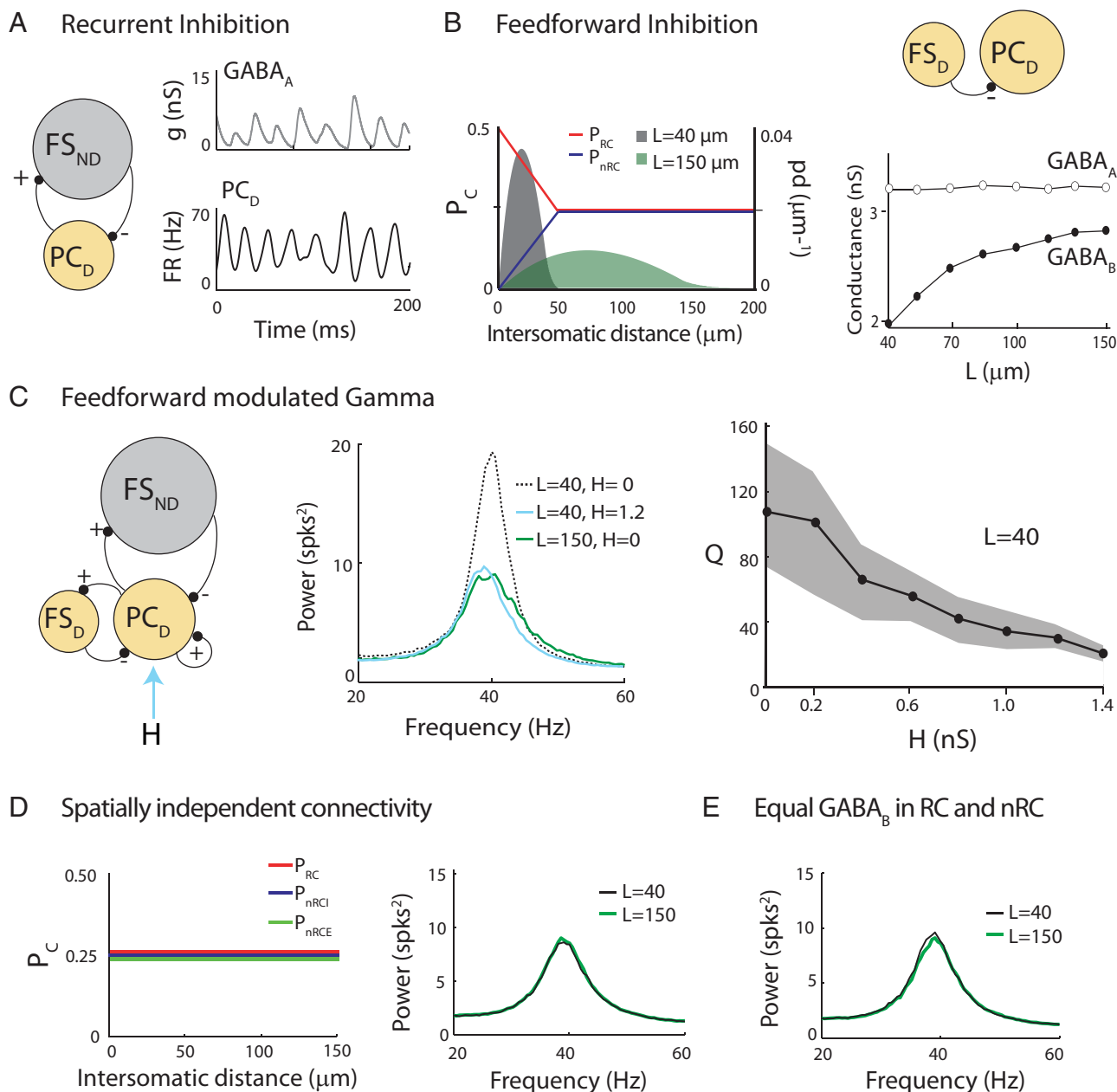
Figure 8. Feedforward inhibition gates the gamma oscillation. ***A***, The driven PCs and nondriven FS cells (PC_D–FS_{ND} populations) participate in the gamma rhythm via recurrent excitatory–inhibitory connections. The average $GABA_A$ conductance from the FS_{ND} population received by a single PC_D unit (gray), and the PC_D network instantaneous firing rate (black) show an anticorrelated 40 Hz rhythm. ***B***, The driven FS cell (FS_D) population sends feedforward inhibition to the PC_D population (top). Left, Overlap of the RC/nRC connection probability (Fig. 5*A*) and the probability density, pd, of the intersomatic distance between a pair of randomly chosen PC_D and FS_D cells (shaded area) for $L = 40\ \mu m$ (gray) and $L = 150\ \mu m$ (green). Computing pd is a hypercube line-picking problem with an explicit formula for the square (for details, see http://mathworld.wolfram.com/SquareLinePicking.html). Right, The average $GABA_A$ and $GABA_B$ conductance from the FS_D population to a PC_D unit as a function of *L*. ***C***, A static $GABA_B$ conductance (*H*) applied to the PC_D simulated the extra feedforward $GABA_B$ conductance when $L = 150\ \mu m$. Middle, The power spectrum of the PC_D population for $L = 40$, $H = 1.2$ nS (cyan curve), is comparable with that of the network when $H = 0$, $L = 150\ \mu m$ (green curve). The spectrum of the PC_D population response for $L = 40$, $H = 0$ nS (black dashed curve), is shown for reference. Right, The *Q* factor computed from the spectra of the PC_D population ($L = 40$) decreases with increasing *H*. Shaded areas indicate ± 1 SD computed across 120 realizations of the network connectivity. ***D***, The removal of the spatial profile in RC and nRC connections reduced the oscillatory power and made gamma activity independent of *L*. Left, Flat spatial profile for RC and nRC connections in PC–FS cell circuits. Right, The PC_D population shows lower gamma power that is independent of *L*. ***E***, When $GABA_B$ is equivalent ($\bar{g}_{GB}^{RC} = \bar{g}_{GB}^{nRC} = 0.0229$ nS) in both RC and nRC PC–FS pairs, the PC_D population shows lower gamma power that is independent of *L*.

coupling influences spike train patterning but not firing rate (Van Vreeswijk et al., 1994). Moreover, this result was robust to variation in the ratio of $GABA_B$ at nRC versus RC synapses—when this ratio is varied over a range consistent with experimental values, the selectivity of oscillatory activity for spatially focal inputs is maintained (supplemental Fig. 3, available at www.jneurosci.org as supplemental material). Thus, although the differences in $GABA_B$ at individual synapses are seemingly small, at

the network level, the confluence of spatial profiles in both connectivity and inputs amplifies the influence of differential inhibition on oscillatory activity.

Currently, the mechanisms by which differential $GABA_B$-mediated responses arise are unknown. One possibility is that activity patterns differ in RC and nRC pairs and promote synaptic processes that differentially influence $GABA_B$ receptor activity. For instance, membrane-bound $GABA_B$ receptors can associate

with GABA$_A$ receptors and undergo agonist-induced cointernalization at highly active synapses (Balasubramanian et al., 2004). Postsynaptic activity could also promote (de)phosphorylation of GABA$_B$ receptors and influence membrane stability (Fairfax et al., 2004) while glutamate spillover from nearby excitatory synapses may decrease the expression of GABA$_B$ receptors (Vargas et al., 2008). Alternatively, differential GABA transporter activity could affect the availability of GABA to perisynaptic GABA$_B$ receptors (Bernstein and Quick, 1999; Gonzalez-Burgos et al., 2009). Additional insight could be provided by studies that address mechanisms by which network activity influences postsynaptic GABA$_B$ inhibitory responses.

Spatial scales of ACx processing

In mice, primary ACx is tonotopically organized in isofrequency bands that are centered at the best frequencies (BFs) and range from 100 to 300 μm in width (rostral–caudal) and up to 600 μm in length (dorsal–ventral) (Stiebler et al., 1997). Within an isofrequency contour, neurons are further clustered according to narrow/broad frequency tuning, intensity tuning, responses to stimulus periodicity or binaural inputs, and response latencies (for review, see Schreiner et al., 2000; Schreiner and Winer, 2007). Our data and model suggest that L2/3 responses are influenced by inputs that range from 50 to 100 μm. In the thalamorecipient layers (L3–L5) that provide input to L2/3 (Wallace et al., 1991), these small scales may reflect subregions of isofrequency bands that are either narrowly tuned or selectively activated by optimal combinations of frequency and other stimulus attributes such as intensity or location. Alternatively, L2/3 neurons in primary ACx receive nearby, long-range and contralateral connections from other auditory areas (Winer, 1984, 1985; Code and Winer, 1985; Ojima et al., 1991; Budinger et al., 2000) and sensory cortices (Budinger et al., 2006). Small-scale activation areas could represent a spatially narrow convergence of these inputs with feedforward drive. Finally, despite the extensive and overlapping projections of the axonal and dendritic arbors, connectivity can be highly specific (Dantzker and Callaway, 2000; Shepherd and Svoboda, 2005; Song et al., 2005; Yoshimura and Callaway, 2005). In particular, RC FS–PC pairs in L2/3 of V1 have a high probability of receiving common input from L4 (Yoshimura and Callaway, 2005), suggesting that selective, feedforward activation of RC pairs is also possible.

There is evidence to support the prediction that the spatial scale of inputs influences gamma band activity. Gamma band activity is strongest when evoked by pure tone stimuli at the BF and decreases for off-BF tones (Brosch et al., 2002). Moreover, correlated neural activity decreases with spatial distance (Brosch et al., 2002) between recording sites as well as for off-BF tones (Brosch and Schreiner, 1999; Brosch et al., 2002). In contrast, click stimuli, which contain a range of frequencies and likely drive a spatially broad area of ACx, disrupt ongoing gamma oscillations (MacDonald and Barth, 1995). One caveat is that the distance between recording electrodes ($\sim$300 μm) limits the spatial resolution of these measurements.

Optical imaging and stimulation allow for the analysis and control of network activity *in vivo* with higher spatial resolution. For instance, in barrel cortex, calcium imaging in L2/3 has shown that stimulus-evoked synchronous activity declines substantially within 100 μm of the column center (Kerr et al., 2007) and neurons separated by <50 μm can have different receptive field properties (Sato et al., 2007). Furthermore, targeted channelrhodopsin-2 expression and light activation of FS–PC networks can induce gamma band oscillatory activity in L2/3

(Cardin et al., 2009). These techniques, in combination with acoustic stimulation, could further elucidate roles for the spatial profile of cortical microcircuits during auditory processing.

Gamma oscillations in cortical processing

Gamma band activity has been observed in the superficial cortical layers of ACx both *in vivo* and *in vitro* (Barth and MacDonald, 1996; Metherate and Cruikshank, 1999; Sukov and Barth, 2001). In addition, gamma oscillations in ACx are modulated by attention (Lakatos et al., 2004), cross-modal activation of somatosensory (Lakatos et al., 2007) or visual inputs (Schroeder et al., 2008), and during learned discrimination tasks (Jeschke et al., 2008). However, the function of gamma oscillations during auditory processing remains unclear.

There are numerous postulated roles for oscillations and synchrony in cortical processing (Buzsáki and Draguhn, 2004; Sejnowski and Paulsen, 2006). Neural populations may interact and organize activity through network oscillations (Fries, 2005). Oscillations could promote synchronous activity in presynaptic populations that enhances postsynaptic responses (Salinas and Sejnowski, 2001) and signal propagation in feedfoward networks (Reyes, 2003). Alternatively, oscillations may provide a clock for phase-based codes (Hopfield, 1995) and reduce spike time variability to improve population discrimination tasks (Masuda and Doiron, 2007; Mazzoni et al., 2008). In all cases, the modulation of oscillatory activity by feedforward or feedback pathways is essential for the dynamic adjustment of cortical responses. Our study gives a potential mechanism whereby the arrangement of cortical circuits permits the spatial distribution of cortical inputs, to modulate synchronous oscillations across the ACx network.

References

Atencio CA, Schreiner CE (2008) Spectrotemporal processing differences between auditory cortical fast-spiking and regular-spiking neurons. J Neurosci 28:3897–3910.

Balasubramanian S, Teissére JA, Raju DV, Hall RA (2004) Hetero-oligomerization between GABAA and GABAB receptors regulates GABAB receptor trafficking. J Biol Chem 279:18840–18850.

Barth DS, MacDonald KD (1996) Thalamic modulation of high-frequency oscillating potentials in auditory cortex. Nature 383:78–81.

Beierlein M, Gibson JR, Connors BW (2003) Two dynamically distinct inhibitory networks in layer 4 of the neocortex. J Neurophysiol 90:2987–3000.

Bernstein EM, Quick MW (1999) Regulation of gamma-aminobutyric acid (GABA) transporters by extracellular GABA. J Biol Chem 274:889–895.

Börgers C, Kopell N (2005) Effects of noisy drive on rhythms in networks of excitatory and inhibitory neurons. Neural Comput 17:557–608.

Börgers C, Epstein S, Kopell NJ (2005) Background gamma rhythmicity and attention in cortical local circuits: a computational study. Proc Natl Acad Sci U S A 102:7002–7007.

Brosch M, Schreiner CE (1999) Correlations between neural discharges are related to receptive field properties in cat primary auditory cortex. Eur J Neurosci 11:3517–3530.

Brosch M, Budinger E, Scheich H (2002) Stimulus-related gamma oscillations in primate auditory cortex. J Neurophysiol 87:2715–2725.

Brown JT, Davies CH, Randall AD (2007) Synaptic activation of GABA(B) receptors regulates neuronal network activity and entrainment. Eur J Neurosci 25:2982–2990.

Brunel N, Wang XJ (2003) What determines the frequency of fast network oscillations with irregular neural discharges? I. Synaptic dynamics and excitation-inhibition balance. J Neurophysiol 90:415–430.

Budinger E, Heil P, Scheich H (2000) Functional organization of auditory cortex in the Mongolian gerbil (*Meriones unguiculatus*). III. Anatomical subdivisions and corticocortical connections. Eur J Neurosci 12:2425–2451.

Budinger E, Heil P, Hess A, Scheich H (2006) Multisensory processing via early cortical stages: connections of the primary auditory cortical field with other sensory systems. Neuroscience 143:1065–1083.

Buhl EH, Tamás G, Fisahn A (1998) Cholinergic activation and tonic excitation induce persistent gamma oscillations in mouse somatosensory cortex in vitro. J Physiol 513:117–126.

Buonomano DV, Merzenich MM (1998) Net interaction between different forms of short-term synaptic plasticity and slow-IPSPs in the hippocampus and auditory cortex. J Neurophysiol 80:1765–1774.

Buzsáki G, Draguhn A (2004) Neuronal oscillations in cortical networks. Science 304:1926–1929.

Cardin JA, Carlén M, Meletis K, Knoblich U, Zhang F, Deisseroth K, Tsai LH, Moore CI (2009) Driving fast-spiking cells induces gamma rhythm and controls sensory responses. Nature 459:663–667.

Code RA, Winer JA (1985) Commissural neurons in layer III of cat primary auditory cortex (AI): pyramidal and non-pyramidal cell input. J Comp Neurol 242:485–510.

Connors BW, Malenka RC, Silva LR (1988) Two inhibitory postsynaptic potentials, and GABAA and GABAB receptor-mediated responses in neocortex of rat and cat. J Physiol 406:443–468.

Cruikshank SJ, Rose HJ, Metherate R (2002) Auditory thalamocortical synaptic transmission in vitro. J Neurophysiol 87:361–384.

Cunningham MO, Whittington MA, Bibbig A, Roopun A, LeBeau FE, Vogt A, Monyer H, Buhl EH, Traub RD (2004) A role for fast rhythmic bursting neurons in cortical gamma oscillations in vitro. Proc Natl Acad Sci U S A 101:7152–7157.

Dantzker JL, Callaway EM (2000) Laminar sources of synaptic input to cortical inhibitory interneurons and pyramidal neurons. Nat Neurosci 3:701–707.

Doiron B, Chacron MJ, Maler L, Longtin A, Bastian J (2003) Inhibitory feedback required for network oscillatory responses to communication but not prey stimuli. Nature 421:539–543.

Dumitriu D, Cossart R, Huang J, Yuste R (2007) Correlation between axonal morphologies and synaptic input kinetics of interneurons from mouse visual cortex. Cereb Cortex 17:81–91.

Fairfax BP, Pitcher JA, Scott MG, Calver AR, Pangalos MN, Moss SJ, Couve A (2004) Phosphorylation and chronic agonist treatment atypically modulate GABAB receptor cell surface stability. J Biol Chem 279:12565–12573.

Fries P (2005) A mechanism for cognitive dynamics: neuronal communication through neuronal coherence. Trends Cogn Sci 9:474–480.

Gonchar Y, Burkhalter A (1999) Differential subcellular localization of forward and feedback interareal inputs to parvalbumin expressing GABAergic neurons in rat visual cortex. J Comp Neurol 406:346–360.

Gonzalez-Burgos G, Rotaru DC, Zaitsev AV, Povysheva NV, Lewis DA (2009) GABA transporter GAT1 prevents spillover at proximal and distal GABA synapses onto primate prefrontal cortex neurons. J Neurophysiol 101:533–547.

Gray CM, Singer W (1989) Stimulus-specific neuronal oscillations in orientation columns of cat visual cortex. Proc Natl Acad Sci U S A 86:1698–1702.

Gupta A, Wang Y, Markram H (2000) Organizing principles for a diversity of GABAergic interneurons and synapses in the neocortex. Science 287:273–278.

Hasenstaub A, Shu Y, Haider B, Kraushaar U, Duque A, McCormick DA (2005) Inhibitory postsynaptic potentials carry synchronized frequency information in active cortical networks. Neuron 47:423–435.

Holmgren C, Harkany T, Svennenfors B, Zilberter Y (2003) Pyramidal cell communication within local networks in layer 2/3 of rat neocortex. J Physiol 551:139–153.

Hopfield JJ (1995) Pattern recognition computation using action potential timing for stimulus representation. Nature 376:33–36.

Hormuzdi SG, Pais I, LeBeau FE, Towers SK, Rozov A, Buhl EH, Whittington MA, Monyer H (2001) Impaired electrical signaling disrupts gamma frequency oscillations in connexin 36-deficient mice. Neuron 31:487–495.

Jeschke M, Lenz D, Budinger E, Herrmann CS, Ohl FW (2008) Gamma oscillations in gerbil auditory cortex during a target-discrimination task reflect matches with short-term memory. Brain Res 1220:70–80.

Johansson S, Druzin M, Haage D, Wang MD (2001) The functional role of a bicuculline-sensitive Ca^{2+}-activated K^+ current in rat medial preoptic neurons. J Physiol 532:625–635.

Jones MS, Barth DS (2002) Effects of bicuculline methiodide on fast (>200 Hz) electrical oscillations in rat somatosensory cortex. J Neurophysiol 88:1016–1025.

Kerr JN, de Kock CP, Greenberg DS, Bruno RM, Sakmann B, Helmchen F

(2007) Spatial organization of neuronal population responses in layer 2/3 of rat barrel cortex. J Neurosci 27:13316–13328.

Lakatos P, Szilágyi N, Pincze Z, Rajkai C, Ulbert I, Karmos G (2004) Attention and arousal related modulation of spontaneous gamma-activity in the auditory cortex of the cat. Brain Res Cogn Brain Res 19:1–9.

Lakatos P, Shah AS, Knuth KH, Ulbert I, Karmos G, Schroeder CE (2005) An oscillatory hierarchy controlling neuronal excitability and stimulus processing in the auditory cortex. J Neurophysiol 94:1904–1911.

Lakatos P, Chen CM, O'Connell MN, Mills A, Schroeder CE (2007) Neuronal oscillations and multisensory interaction in primary auditory cortex. Neuron 53:279–292.

Laurent G, Wehr M, Davidowitz H (1996) Temporal representations of odors in an olfactory network. J Neurosci 16:3837–3847.

MacDonald KD, Barth DS (1995) High frequency (gamma-band) oscillating potentials in rat somatosensory and auditory cortex. Brain Res 694:1–12.

Markram H, Wang Y, Tsodyks M (1998) Differential signaling via the same axon of neocortical pyramidal neurons. Proc Natl Acad Sci U S A 95:5323–5328.

Masuda N, Doiron B (2007) Gamma oscillations of spiking neural populations enhance signal discrimination. PLoS Comput Biol 3:e236.

Mazzoni A, Panzeri S, Logothetis NK, Brunel N (2008) Encoding of naturalistic stimuli by local field potential spectra in networks of excitatory and inhibitory neurons. PLoS Biol 4:e1000239.

Metherate R, Cruikshank SJ (1999) Thalamocortical inputs trigger a propagating envelope of gamma-band activity in auditory cortex in vitro. Exp Brain Res 126:160–174.

Morita K, Kalra R, Aihara K, Robinson HP (2008) Recurrent synaptic input and the timing of gamma-frequency-modulated firing of pyramidal cells during neocortical "UP" states. J Neurosci 28:1871–1881.

Ojima H, Honda CN, Jones EG (1991) Patterns of axon collateralization of identified supragranular pyramidal neurons in the cat auditory cortex. Cereb Cortex 1:80–94.

Oswald AM, Reyes AD (2008) Maturation of intrinsic and synaptic properties of layer 2/3 pyramidal neurons in mouse auditory cortex. J Neurophysiol 99:2998–3008.

Reyes A, Lujan R, Rozov A, Burnashev N, Somogyi P, Sakmann B (1998) Target-cell-specific facilitation and depression in neocortical circuits. Nat Neurosci 1:279–285.

Reyes AD (2003) Synchrony-dependent propagation of firing rate in iteratively constructed networks in vitro. Nat Neurosci 6:593–599.

Salinas E, Sejnowski TJ (2001) Correlated neuronal activity and the flow of neural information. Nat Rev Neurosci 2:539–550.

Sato TR, Gray NW, Mainen ZF, Svoboda K (2007) The functional microarchitecture of the mouse barrel cortex. PLoS Biol 5:e189.

Schreiner CE, Winer JA (2007) Auditory cortex mapmaking: principles, projections, and plasticity. Neuron 56:356–365.

Schreiner CE, Read HL, Sutter ML (2000) Modular organization of frequency integration in primary auditory cortex. Annu Rev Neurosci 23:501–529.

Schroeder CE, Lakatos P, Kajikawa Y, Partan S, Puce A (2008) Neuronal oscillations and visual amplification of speech. Trends Cogn Sci 12:106–113.

Sejnowski TJ, Paulsen O (2006) Network oscillations: emerging computational principles. J Neurosci 26:1673–1676.

Shepherd GM, Svoboda K (2005) Laminar and columnar organization of ascending excitatory projections to layer 2/3 pyramidal neurons in rat barrel cortex. J Neurosci 25:5670–5679.

Song S, Sjöström PJ, Reigl M, Nelson S, Chklovskii DB (2005) Highly nonrandom features of synaptic connectivity in local cortical circuits. PLoS Biol 3:e68.

Stepanyants A, Hirsch JA, Martinez LM, Kisvárday ZF, Ferecskó AS, Chklovskii DB (2008) Local potential connectivity in cat primary visual cortex. Cereb Cortex 18:13–28.

Stepanyants A, Martinez LM, Ferecskó AS, Kisvárday ZF (2009) The fractions of short- and long-range connections in the visual cortex. Proc Natl Acad Sci U S A 106:3555–3560.

Stiebler I, Neulist R, Fichtel I, Ehret G (1997) The auditory cortex of the house mouse: left-right differences, tonotopic organization and quantitative analysis of frequency representation. J Comp Physiol A 181:559–571.

Sukov W, Barth DS (2001) Cellular mechanisms of thalamically evoked gamma oscillations in auditory cortex. J Neurophysiol 85:1235–1245.

Sun QQ, Huguenard JR, Prince DA (2006) Barrel cortex microcircuits: thalamocortical feedforward inhibition in spiny stellate cells is mediated by a small number of fast-spiking interneurons. J Neurosci 26:1219–1230.

Swadlow HA (2003) Fast-spike interneurons and feedforward inhibition in awake sensory neocortex. Cereb Cortex 13:25–32.

Thomson AM, Lamy C (2007) Functional maps of neocortical local circuitry. Front Neurosci 1:19–42.

Thomson AM, West DC, Hahn J, Deuchars J (1996) Single axon IPSPs elicited in pyramidal cells by three classes of interneurones in slices of rat neocortex. J Physiol 496:81–102.

Thomson AM, West DC, Wang Y, Bannister AP (2002) Synaptic connections and small circuits involving excitatory and inhibitory neurons in layers 2–5 of adult rat and cat neocortex: triple intracellular recordings and biocytin labelling in vitro. Cereb Cortex 12:936–953.

Van Vreeswijk C, Abbott LF, Ermentrout GB (1994) When inhibition not excitation synchronizes neural firing. J Comput Neurosci 1:313–321.

Vargas KJ, Terunuma M, Tello JA, Pangalos MN, Moss SJ, Couve A (2008) The availability of surface GABAB receptors is independent of GABA but controlled by glutamate in central neurons. J Biol Chem 283:24641–24648.

Wallace MN, Kitzes LM, Jones EG (1991) Intrinsic inter- and intralaminar connections and their relationship to the tonotopic map in cat primary auditory cortex. Exp Brain Res 86:527–544.

Winer JA (1984) The pyramidal neurons in layer III of cat primary auditory cortex (AI). J Comp Neurol 229:476–496.

Winer JA (1985) Structure of layer II in cat primary auditory cortex (AI). J Comp Neurol 238:10–37.

Yoshimura Y, Callaway EM (2005) Fine scale specificity of cortical networks depends on inhibitory cell type and connectivity. Nat Neurosci 8:1552–1559.